https://doi.org/10.5194/egusphere-2023-1224
Preprint. Discussion started: 9 June 2023

Role of thermodynamic and turbulence processes on the fog life cycle during SOFOF3D experiment

Cheikh DIONE[1*], Martial HAEFFELIN[1], Frederic BURNET[2], Christine LAC[2], Guylaine CANUT[2], Julien DELANOË[3], Jean-Charles DUPONT[4], Susana JORQUERA[3], Pauline MARTINET[2], Jean-Francois RIBAUD[5], and Felipe TOLEDO[3]

1) Institut Pierre Simon Laplace, CNRS, Ecole Polytechnique de Paris, Institut Polytechnique de Paris, Paris, France
2) Meteo-France, Toulouse, France
3) Laboratoire Atmosphères, Milieux, Observations Spatiales/UVSQ/CNRS/UPMC, 78280 Guyancourt, France
4) Institut Pierre-Simon Laplace, École Polytechnique, UVSQ, Université Paris-Saclay, 91128 Palaiseau, France
5) Laboratoire de Météorologie Dynamique, École Polytechnique, 91128 Palaiseau, France.
* corresponding author: Cheikh DIONE, cdione@ipsl.fr

Abstract:

In this study, we use a synergy of in-situ and remote sensing measurements collected during the Southwest FOGs 3D experiment for processes study (SOFOG3D) field campaign in autumn 2019 and winter 2020, to analyze the thermodynamic and turbulence processes related to fog formation, evolution, and dissipation across southwestern France. Based on a unique dataset with a very high resolution and a fog conceptual model, an analysis of the four heaviest fog episodes (two radiation fogs and two advection-radiation fogs) is conducted. The results show that radiation and advection-radiation fogs form under deep and thin temperature inversion, respectively. For both fog categories, the transition period from stable to adiabatic fog and the fog adiabatic phase are driven by vertical mixing associated with an increase in turbulence in the fog layer due to mechanical production (turbulence kinetic energy (TKE) up to 0.4 $m^2 s^{-2}$ and vertical velocity variance (σ_w^2) up to 0.04 $m^2 s^{-2}$) generated by brisk wind at the supersite (advection). The dissipation time is observed at night for the advection-radiation fog case studies and during the day for the radiation fog case studies. Night-time dissipation is driven by horizontal advection generating mechanical turbulence (TKE at least 0.3 $m^2 s^{-2}$ and σ_w^2 larger than 0.04 $m^2 s^{-2}$). Daytime dissipation is linked to the combination of thermal and mechanical turbulence related respectively to solar heating (near surface sensible heat flux larger than 10 W m^{-2}) and advection. Through a deficit of the fog reservoir of liquid water path, the fog conceptual model estimates the dissipation time at least one hour before the observed dissipation for radiation fog cases. It gives a better estimate of the fog dissipation time for advection-radiation cases. This study also demonstrates the importance of using instrumental synergy (with microwave radiometer, wind lidar, weather station, and cloud radar) and a fog conceptual model to better predict fog characteristics and dissipation time at nowcasting ranges.

Key words: Fog conceptual model, radiation/advection fog, fog life cycle, turbulence, Southwestern France, SOFOG3D

https://doi.org/10.5194/egusphere-2023-1224
Preprint. Discussion started: 9 June 2023

1. Introduction

Fog is an extreme meteorological phenomenon forming in several regions of earth under different atmospheric conditions depending on the season and location (Gultepe et al., 2007). It is defined by the suspension of water droplets in the lowest troposphere which reduces the horizontal visibility to lower or at least 1000 m. Fog has significant negative impacts on air, road and marine traffic causing large economical and human losses (Bartok et al., 2012, Bartoková et al., 2015, Huang and Chen, 2016). It also has a high impact on solar energy, particularly in the mid-latitudes during Autumn and Winter. Based on in-situ measurements, several studies have focused on fog formation at different regions and highlighted the main processes leading to its initiation allowing to define four categories of fog: radiation fog (Price 2019), advection-radiation fog (Gultepe et al., 2007, 2009; Niu et al., 2010a, b, Dupont et al., 2012), advection fog (Koračin et al., 2014; Liu et al., 2016, Fernando et al., 2021), and precipitation fog (Tardif and Rasmussen, 2007; Liu et al., 2012). According to the literature, several processes are identified to drive fog evolution and dissipation depending on each category. Fog formation requires low intensity of turbulence (Nakanishi 2000; Bergot 2013; Price 2019)

Dhangar et al., 2021 found that optically thin fog develops under low-turbulence kinetic energy and the transition to dense fog is observed when the turbulence increases and reaches enough values to allow the vertical mixing of the fog layer. The dissipation of radiation fog is usually observed after sunrise and linked with the increase in solar heating leading to the evaporation of water drops and a vertical mixing of water vapor (Roach, 1995; Haeffelin et al., 2010; Maalick et al., 2016). Bergot et al., 2015 relied on large eddy simulations (LES) to characterize the role of dry downdrafts in allowing solar radiation to reach the ground and increasing the turbulence. Additionally, Pauli et al., 2022 studied the climatology of fog and low stratus cloud formation and dissipation times in Central Europe using satellite data and showed that fog dissipation is also often related to topography. The dissipation processes are more difficult to study then the fog formation processes, due to the complexity of fog's scale. At the state of the art, based on case studies, numerical weather prediction models (Philip et al., 2016, Bell et al., 2022) and high resolution models (Price et al., 2018, Ducongé et al., 2020, Fathalli et al., 2022) up to LES (Bergot et al., 2015, Mazoyer et al., 2017) have the ability to simulate fog formation in several complex areas. However, they have difficulties in simulating the processes driving fog evolution over land in real time (Steeneveld *et al.*, 2015, Price et al., 2015, Román-Cascón et al., 2016; Wærsted et al., 2019; Pithani et al., 2020, Boutle *et al.*, 2022).

https://doi.org/10.5194/egusphere-2023-1224
Preprint. Discussion started: 9 June 2023

Toledo et al., 2021 developed a one-column conceptual model of adiabatic continental fog allowing to define key fog metrics as the equivalent fog adiabaticity by closure and the reservoir of liquid water path (RLWP) that can be estimated in real-time and allowing a diagnostic of fog evolution. Based on seven years of measurements collected at SIRTA (Site Instrumental de Recherche par Télédétection Atmosphérique), a French observatory located at Palaiseau/France, Toledo et al., 2021 have validated their model on the timing of fog dissipation based on the RLWP. The limitation of this model is that the estimation of the reservoir depends on fog specific parameters and does not take into account local (turbulence) or large scale processes (advection). Indeed, to further understand uncertainties associated with the estimation of the RLWP, the validation of the model using data from other measurement sites having a large occurrence of fog is another step before using it in nowcasting ranges.

Understanding the life cycle of fog is an imperative for numerical weather prediction models in order to set up an effective and efficient early warning system to reduce the socio-economic impacts of this phenomenon in areas with high occurrence of fog. Thus, finding the right instruments on which this warning system will be based is also another challenge that can be partly resolved by field campaigns combining both in-situ and remote sensing measurements and numerical simulations. At the state of the art, nowcasting fog requires more efforts in in-situ measurements and modeling. In this context, the SOuth westFOGs 3D (SOFOG3D) project, led by Météo-France, was designed to document local processes involved in fog formation, evolution and dissipation to better improve its predictability in numerical weather prediction models in the Southwestern France.

In order to improve our understanding of the processes driving the fog life cycle and to validate the fog conceptual model from Toledo et al., 2021 on another region than the one on which it has been developed, the current study aims at identifying the main dynamical and thermodynamic processes driving fog's formation, evolution, and dissipation in the framework of SOFOG3D project. Using an instrumental synergy of in-situ and remote sensing measurements and the fog conceptual model, the phenomenology of fog and the different phases driving its evolution are deeply analyzed considering four heavy fog case studies observed over Southern France during Winter 2019-2020.

This paper is structured into five sections. The datasets and methodological approach are described in the following section. Section 3 gives an analysis of the processes involved in fog evolution based on two different categories of fog formation phenomenology. Section 4 of this

https://doi.org/10.5194/egusphere-2023-1224
Preprint. Discussion started: 9 June 2023

manuscript includes a discussion on the thermodynamical and turbulent processes driving the fog phases and Section 5 presents the conclusion.

2. Data and methodology

In a mesoscale context, the SOFOG3D field experiment is located in Southwestern France, in the Aquitaine region (Fig. 1a). The field campaign was carried out during the Autumn 2019 and Winter 2020 period leading to 15 intensive observation periods (IOPs). A unique dataset has been collected across a complex region with a very contrasted topography. This region is bordered in the east by the “Massif Central”, in the west by the Atlantic Ocean, in the north by Bordeaux and in the south by the “Pyrenees”. In the region, several dynamical effects can be observed such as sea breeze, land breeze, and mesoscale foehn circulations influencing the fog life cycle. At the local scale, the supersite under focused here is bordered by two rivers: “La Garonne” to the East and “L’Eyre” to the west (Fig. 1a). These two rivers and the surrounding surface heterogeneities can modulate the fog formation and dissipation times. During the campaign, several in-situ and remote sensing measurements were jointly deployed in the studied area of SOFOG3D. In this paper, our analysis focuses on the data collected in the surroundings of the supersite at Charbonnière, the most instrumented site (Fig. 1b) during the field campaign. Below, the descriptions of the in-situ and remote sensing measurements and then the fog conceptual model are presented with emphasis on the main meteorological variables used in the study.

2.1 Dataset

2.1.1 Surface measurement data

A network of surface weather stations was installed in the study domain of SOFOG3D at the vicinity of Charbonnière, to document the spatial variability of fog and surface heterogeneities at the local scale (Fig. 1b). Four weather stations were also deployed around the supersite in a northeast-southwest transect (Fig. 1b). These stations were installed at Moustey, Cape Sud, Tuzan and Noaillan, almost at the same altitude, and operated continuously with very high temporal resolution (0.1 s time interval) during the period from 18 October 2019 to 31 December 2020. In addition to temperature, pressure, relative humidity sensors and anemometer, a scatterometer provided the visibility used to estimate fog formation and dissipation times at each station. Temperature data are used to characterize the spatial variability of the radiative cooling. Wind

https://doi.org/10.5194/egusphere-2023-1224
Preprint. Discussion started: 9 June 2023

speed and direction are used to get an indication of the local circulations and their association with air mass advection (spatial coherence of wind) and source of turbulence.

In this study, fog occurrence is defined using the visibility at the supersite based on an algorithm developed by Tardif and Rasmussen, 2007. This algorithm consists of dividing visibility time series into 10 min blocks. A fog block means that half of the visibility measurements during a 10 min period are below 1000 m. Blocks are characterized by a positive or negative construct. A positive construct indicates that five consecutive blocks of which the central block is fog and at least two other blocks are also fog blocks. The opposite means a negative construct. Thus, the fog formation time corresponds to the first fog block in the first positive construct encountered. The fog dissipation time corresponds to the last fog block in the last positive construct before either a negative construct or three consecutive non-fog blocks are encountered. This algorithm discards fog events shorter than 1 hour.

Meteo-France installed in a fallow field near the supersite, several sensors as Licor analyzers and sonic anemometers to continuously measure the near-surface (3 m a.g.l) meteorological conditions (air temperature and relative humidity) and pressure at 0.3 m a.g.l) and the three components of the wind at 10 m a.g.l. These instruments provided high frequency data at 20 Hz. In this study, to document fog dissipation processes, we use sensible heat flux (SHF), turbulence kinetic energy (TKE), and vertical velocity variance (σ_w^2). These variables are estimated using the Eddy-covariance methods (Foken et al., 2004, Mauder et al., 2013) calculated every 30 minutes after a high quality control of the data. More details on the data can be found in Canut, 2020.

2.1.2 Observation of cloud characteristics

For the monitoring of cloud layers, a BASTA cloud radar (Delanoë et al., 2016) was deployed at Charbonnière and a CL51 Ceilometer at Tuzan (7.4 km northwest of Charbonnière) (Fig. 1b).

BASTA is a 95-GHz cloud radar manufactured by the Laboratoire Atmosphères, Milieux, Observations Spatiales (LATMOS) with an absolute calibration method for frequency-modulated continuous wave (FMCW) cloud radars based on corner reflectors (Toledo et al., 2020). From 7 November 2019 to 12 March 2020, the radar was operated continuously with a vertical pointing mode having three vertical resolutions (12.5 m, 25 m, and 100 m). It provided radar reflectivity and Doppler velocity. The lowest mode, having its first available gate at 37.5 m a.g.l and 12.5 m of vertical resolution, is used to estimate the cloud top height (CTH) which gives the fog thickness at a time resolution of 30 seconds. It also provides the level of highest concentration of droplets in the fog layer. The CTH is estimated using a radar reflectivity threshold of -34 dBZ.

The CL51 is manufactured by Vaisala and automatically provided three estimates of cloud base height (CBH) allowing the detection of cloud decks every 30 seconds with a vertical resolution of 15 m. from 10 October 2019 to 2 April 2020. In this study, we use the lowest CBH, which corresponds to the base height of stratus cloud lowering or lifting when fog forms or dissipates, respectively. More information on the data provided by the CL51 can be found in Burnet, 2021.

2.1.3 Temperature and wind profiling

A microwave radiometer Hatpro (MWR) manufactured by Radiometer Physics GmbH (RPG) was installed at the supersite to characterize thermodynamic atmospheric conditions during the field campaign. From 4 December 2019 to 9 May 2020, the MWR operated continuously at the supersite using two spectral-bands: the K-band which 22.24-31 GHz used for the retrieval of humidity profiles, integrated water vapor (IWV) content and liquid water path (LWP), and the V-band which 51-58 GHz to retrieve temperature profiles. In order to improve the vertical resolution in the boundary layer, the MWR was set up to scan in 10 elevation angles every 10 minutes with a zenith pointing each 1 second. Using neural networks, brightness temperatures measured by the MWR are inverted to temperature and humidity variables. More details on this method can be found in Martinet et al., 2022. Comparing temperature and humidity profiles retrieved by the MWR with radiosonde data, Martinet et al., 2022 found that air temperature has cold biases below 0.5 K in absolute value below 2 km but increases up to 1.5 K above 4 km altitude. The low biases in the lowest atmosphere allow a good estimation of the lowest temperature inversion under focus in this study. For each case study, the transition from stable to adiabatic fog is estimated using the static atmospheric stability in the lowest atmosphere computed using the temperature profile. The air temperature profiles are also used to characterize the atmospheric conditions linked to the development of fog at Charbonnière. For the absolute humidity, the maximum dry bias of the MWR is around 1.4 g m^{-3} in the lowest troposphere up to 1.7 km and becomes wet above (0.3 g m^{-3}). The small biases in humidity profiles shows that the LWP accuracy is in the scope of those defined in the literature (Crewell and Löhnert, 2003; Marke et al., 2016). The LWP is a key parameter to consider for the microphysical characteristics of fog and is used in the conceptual model. More information regarding the data can be found in Martinet, 2021.

https://doi.org/10.5194/egusphere-2023-1224
Preprint. Discussion started: 9 June 2023

The WindCube lidar becomes a common instrument used in documenting very low atmospheric phenomena such as turbulence (Liao et al., 2020; Kumer et al., 2016). Dias Neto et al., 2023 demonstrated the usefulness of the wind speed and direction estimated using the WindCube V2. Comparing wind from WindCube V2 with GPS radiosonde, they found low biases of 0.52 m s^{-1} and 0.37° for the wind speed and direction, respectively. To investigate the dynamics of the atmosphere at the supersite, a WindCube V2 lidar manufactured by Leosphere was deployed by Meteo-France during the field campaign to provide from 1 October 2019 to 10 April 2020, the wind measurements at 10 levels ranging from 40 m to 220 m above ground level (a.g.l). The measurements made at a 1 Hz frequency and a 20 m vertical resolution provided the estimation of turbulence parameters such as the turbulent kinetic energy (TKE). The TKE is computed every 30 minutes using the horizontal wind component at the high resolution. It is used in this study to analyze the role of turbulence within the foggy-layer to further characterize fog formation, evolution, and dissipation. More details on the WindCube lidar data can be found in Canut et al., 2022.

2.1.4 Fog adiabaticity and reservoir

To further understand fog characteristics, it is essential to focus our analysis on several variables related to the formation, evolution and dissipation of fog. Fog adiabaticity and reservoir are key metrics driving the life cycle of fog. They are estimated using the fog conceptual model (Toledo et al., 2021) developed at SIRTA. This model is a uni-dimensional model inspired by previous numerical models for stratus clouds (Betts, 1982, Albrecht et al., 1990; and Cermak and Bendix, 2011). The basic hypothesis is to consider a well-mixed fog layer and to express the increase in height of the fog liquid water content as a function of the local adiabaticity and the negative of the change in the saturation mixing ratio with height ($\Gamma_{ad}(T,P)$) (equation A1). Fog liquid water path is parameterized as a function depending on the equivalent fog adiabaticity (α_{eq}) and the CTH (equation A3). The equivalent fog adiabaticity is used to characterize the buoyancy in low clouds. α_{eq} varies depending on the in-cloud mixing parameter β and is expressed as $\alpha_{eq} = (1\text{-}\beta)$ (Betts, 1982 and Cermak and Bendix, 2011). For low-level clouds, as stratus and stratocumulus, α_{eq} is between 0.6 and 0.9 (Braun et al., 2018) indicating sufficient buoyancy in the cloud layer with an adiabatic profile. To parameterize this parameter in the fog conceptual model, Toledo et al., 2021 used an inversion of Eq. (A3) to define a fog adiabaticity from closure ($\alpha_{eq}^{closure}$) given in equation (1). $\alpha_{eq}^{closure}$ depends on the accumulated liquid water content (LWC) at the fog base (LWC_o), fog

https://doi.org/10.5194/egusphere-2023-1224
Preprint. Discussion started: 9 June 2023

thickness (e.g. CTH), the LWP and the adiabaticity. The adiabaticity lapse rate is a function of air temperature and pressure. Toledo et al., 2021 found that the equivalent fog adiabaticity from closure is negative when the LWP is below 30 g m^{-2}. They defined the transition phase from stable to adiabatic conditions when the equivalent fog adiabaticity from closure is around 0.5. In the conceptual model, this parameter is estimated only for a CTH below 462.5 m with free cloud above.

$$\alpha_{eq}^{closure} = \frac{2\left(LWP - LWC_0 CTH\right)}{\Gamma_{ad}\left(T,P\right) CTH^2} \quad (1)$$

Considering that adiabatic fog exists because the liquid water path in its thickness is strictly greater or equal to its critical liquid water path (CLWP) (Toledo et al., 2021), it is possible to define an associated quantity named the fog reservoir of liquid water path (RLWP). The RLWP is defined as the difference between fog current liquid water path and the critical value, as shown in equation 2. It depends on the critical liquid water content (LWCc) (A.4), the adiabaticity and fog thickness. The calculation of fog RLWP can be used to anticipate the dissipation or thickening of the fog in the coming minutes or hours. Based on 20 fog cases at SIRTA, Toledo, 2021 found that for a RLWP > 30 g m^{-2} in a given time instant, fog does not dissipate within the following 30 minutes. He also showed that the RLWP trend decreases before fog dissipation time and increases when fog is persisting. This behavior motivates the analysis of the RLWP trend in this study to improve the characterization of the different fog phases.

$$RLWP = LWP - CLWP = LWP - \frac{1}{2}\alpha_{eq}\Gamma_{ad}\left(T,P\right) CTH^2 - LWC_c CTH \quad (2)$$

The number of fog events observed during the SOFOG3D field campaign is not sufficient to calibrate the fog conceptual model in southeastern France as in SIRTA (Toledo et al., 2021). In this study, we use the model with its parametrization at SIRTA to further characterize the different phases observed in the lifetime of fog based on single identified case studies. The model is performed when the visibility is lower than 1000 m. $\alpha_{eq}^{closure}$ is used to characterize the fog transition from stable phase to adiabatic phase. The RLWP gives information about the predictability of fog dissipation time at nowcasting range. More details on the fog conceptual model is given in appendices and can be found in Toledo, 2021.

2.2 Case studies and methodological approach

For the whole SOFOG3D campaign, based on the fog defined criteria described in section 2.2.1, 31 fog events are identified during 31 October 2019 - 26 March 2020 period. For each one, a

https://doi.org/10.5194/egusphere-2023-1224
Preprint. Discussion started: 9 June 2023

visual expectation of the time-height cross-section of the radar reflectivity from BASTA cloud radar and the cloud base height from the Ceilometer was carried out. We selected the four most developed fog episodes, namely case studies 1 (IOP 5), 2 (IOP 6), 3 (IOP 11) and 4 (IOP 14).

As in Toledo et al., 2021 (their Fig. 3), Figure 2 shows the equivalent adiabaticity by closure versus LWP and CTH for the 4 fog case studied. It indicates that $\alpha_{eq}^{closure}$ researches 0.5 when LWP > 20 g m^{-2} and the CTH > 150 m which should be the conditions favorable for the fog to become optically opaque to the infrared radiation. At the supersite, the LWP observed during that transition is lower than the threshold at SIRTA (LWP > 30 g m^{-2}) (Wærsted et al., 2017 and Toledo et al., 2021). However, there is a consistency between both sites on the computation of the equivalent adiabaticity by closure. This legitimises the choice of the four days, and motivates the use of the $\alpha_{eq}^{closure}$ in this study to define the transition phase between stable and adiabatic fog.

For the selected case studies, Table 1 contains the fog formation and dissipation times, fog formation types, and fog duration at the supersite. For all selected fog events, the formation time of fog is observed between 20:40 and 22:40 UTC and the dissipation time varies from night to daytime. These selected fogs triggered by radiation (2 cases) or advection-radiation (2 cases) processes.

For each selected case study, temperature profiles from the MWR, radar reflectivity profiles from the BASTA cloud radar and the equivalent fog adiabaticity derived from the conceptual model are used to define the four fog phases characterizing the fog evolution: fog pre-onset, stable fog, adiabatic fog, and fog dissipation. Note that an important time of the fog life cycle is the transition time between stable and adiabatic fog. Each fog phase is defined as following:

1/ Fog pre-onset is defined as the two hours preceding fog onset associated with cloud free conditions.

2/ In the four cases studies, the stable phase starts at fog onset. It is characterized by a stable temperature profile in the lowest 100 m of the atmosphere.

3/ The transition time separating the stable and adiabatic phases can be defined differently depending on the meteorological variables considered. Price et al., 2011 defined this transition time as the time when the air temperature is constant in the fog lowest layer (1.5 - 50 m a.g.l). Toledo et al., 2021 found that the transition is observed when the equivalent fog adiabaticity by closure is increasing between 0 and 0.5. In this study, for a better definition of this period, we take into account the static stability given by the hourly profiles of mean air temperature from the MWR, the fog geometry (CTH) from the cloud radar, and the $\alpha_{eq}^{closure}$ from the conceptual model. Indeed, the

https://doi.org/10.5194/egusphere-2023-1224
Preprint. Discussion started: 9 June 2023

transition period is defined as the time when the temperature profile becomes unstable or neutral in the 0-75 m a.g.l layer, while the fog CTH increases with time, and $\alpha_{eq}^{closure}$ increases from 0 to about 0.5. Note that the thickening of the fog is associated with the elevation of the level of the maximum radar reflectivity. The transition phase starts when $\alpha_{eq}^{closure} < 0.5$, the CTH suddenly increases more than 25 m in 5 minutes under a stable or neutral layer. This phase ends when $\alpha_{eq}^{closure}$ reaches 0.5 and the fog layer becomes neutral or unstable.

4/ Fog adiabatic phase is characterized by $\alpha_{eq}^{closure}$ around 0.5, a neutral or unstable temperature profile, and a radar reflectivity that increases with increasing altitude and peaks a few tenths of meters below cloud top.

5/ Fog dissipation phase is defined as being the period between 30 minutes before and after dissipation time (when horizontal visibility becomes greater than 1 km). Since the fog dissipation time does not appear abruptly, as it is driven by thermodynamical processes, we consider this time range to further document them.

Based on these fog phase definitions, in the following, we describe the four case studies. For each fog event, we document, using the fog conceptual model and the instrumental synergy, the processes involved in the evolution of fog in each of these phases, in order to identify the main processes driving the fog life cycle.

Table 1 : *Case study number, fog onsets, type of fog formation, fog dissipation times, fog duration and type of fog dissipation for the four documented case studies. Time is in UTC. Dates are in the format "dd/mm/yyyy". "dd" indicates the day, "mm" the month and "yyyy" the year.*

Case study number	Formation time		Fog types	Dissipation time		Fog duration (hh:min)
	Date dd/mm/yyyy	Hours (UTC)		Date dd/mm/yyyy	Hours (UTC)	
1	28/12/2019	22:40	Radiation	29/12/2019	11:00	12:20
2	05/01/2020	20:40	Radiation	06/01/2020	08:40	12:00
3	08/02/2020	20:40	Advection-radiation	09/02/2020	03:40	7:00
4	07/03/2020	21:20	Advection-radiation	08/03/2020	04:00	6:40

3. Fog formation, evolution, and dissipation processes

3.1 Case study 1 (IOP 5) analysis

https://doi.org/10.5194/egusphere-2023-1224
Preprint. Discussion started: 9 June 2023

Figures 3a and 3b indicate the time-cross sections of the radar reflectivity estimated from BASTA cloud radar during case study 1, on the 28-29 December 2019, respectively up to 600 m and 12000 m. They show a clear sky before fog formation time at 22:40 UTC on 28 December 2019. During fog evolution, cloud free conditions are observed above the fog top height until 09:00 UTC when sparse thin high-altitude clouds occur above the cloud radar. Figure 3c presents a quasi-homogeneous fog formation time between the three sites and heterogeneous dissipation time. At Charbonnière, fog dissipated at 11:00 UTC, on 29 December 2019 and two hours earlier at Noaillan. At all sites, low temperatures below 4 °C (Fig. 3e) are observed during the fog period. Near the surface, light wind (< 1 m s^{-1}) are recorded at all sites from fog pre-onset to fog stable/adiabatic transition times (Fig. 3d and 3f).

The fog pre-onset is marked by a double stratification of the atmospheric boundary layer with a thin inversion from surface up to 100 m and deep and strong inversion (14 °C km^{-1}) above (Fig. 4a). Atmospheric conditions are dominated by an easterly wind that reaches 5 m s^{-1} above 100 m a.g.l which could be considered as a nocturnal low-level jet (Fig. 4d). The mean cooling rate near the surface is -0.9 °C h^{-1}. The strong decrease in temperature is associated with surface radiative cooling (cloud free), negative SHF (-0.23 W m^{-2}) (Fig. 4h), near surface low wind (0.61 m s^{-1}) (Fig. 3d and 3f) and very low thermal turbulence (TKE = 0.18 m^2 s^{-2} and σ_w^2 = 0.002 m^2 s^{-2}). These conditions lead to thermally-stable atmospheric conditions which are favorable for fog formation (Table 1). The fog onset slightly precedes the minimum of SHF.

The fog stable phase lasts around 6 h (22:50 - 05:00 UTC). Near the surface, it is characterized on average by a very low radiative cooling rate (-0.18 °C h^{-1}), an almost zero SHF , an easterly light wind (0.78 m s^{-1}), low turbulence (TKE = 0.12 m^2 s^{-2}, σ_w^2 = 0.01 m^2 s^{-2}), and a negative $\alpha_{eq}^{closure}$ (-1.3) (Fig. 4e), a low LWP of 2.18 g m^{-2} (Fig. 4g), a slight increase in time of the fog thickness up to 50 m, and a relatively stable temperature inversion height. During this phase, turbulence, LWP and RLWP are sufficiently low to maintain thermally-stable fog with an horizontal visibility of 736 m on average.

For this case, the transition time from stable fog to adiabatic fog is observed between 05:00 and 07:00 UTC at the supersite. It corresponds to the lowest visibility (198 m) and is illustrated by a transition in the vertical profiles of air temperature (Fig. 4a) from stable at 05:00 to unstable at 06:00 UTC. The transition is materialized by a deepening of the cold layer. At 05:00 UTC the coldest temperature is at the surface. At 06:00 UTC, the minimum temperature is observed at 50 m a.g.l. At that time, the vertical profile of radar reflectivity increases with height, indicating a vertical

https://doi.org/10.5194/egusphere-2023-1224
Preprint. Discussion started: 9 June 2023

development of fog (Fig. 4b). At the end of this phase, $\alpha_{eq}^{closure}$ reaches 0.5 which is consistent with the threshold obtained at the SIRTA site by Toledo et al., 2021. The mean SHF reaches 4.4 W m^{-2} and around 10 W m^{-2} at the phase end (Fig. 4h). The wind speed at 10 m a.g.l increases to 1.14 m s^{-1} and shifts in direction from East to Southeast. The TKE remains constant and the σ_w^2 significantly increases to 0.01 m^2 s^{-2}. Vertical velocity variance values observed are higher than the threshold fixed by Price et al., 2019 for a thermally-stable surface layer. This increase in turbulence indicates a vertical mixing in the fog layer. The LWP and RLWP peak at the end of the transition phase consistently with a decrease in visibility. Due to the simultaneous increase in SHF, TKE and σ_w^2, the transition phase is driven by both thermal and mechanical turbulence.

The fog adiabatic phase is observed between 07:00 and 11:00 UTC (4 h duration) at the supersite. This phase is characterized by a vertical development of fog up to 185 m (Fig. 4b) and the arrival of sparse high clouds (Fig. 3a and 3b) associated with the lowering of the temperature inversion top height above the fog top (Fig. 4c). Note that these clouds have no effect on the radiative cooling at the top height of the fog. The fog layer becomes warmer (+0.77 °C h^{-1} on average) and its LWP and RLWP reach 26.16 g m^{-2} and +6.38 g m^{-2}, respectively. The turbulence gradually increases in the fog layer (Fig. 4f) (TKE = 0.28 m^2 s^{-2}) due to an increase of the horizontal wind speed (2.4 m s^{-1}) and its shift from southeasterly to easterly (Fig. 4d). In the same way, the vertical velocity variance increases to 0.04 m^2 s^{-2} and is driven by the vertical wind shear and the increase in SHF (12.9 W m^{-2}) (Fig. 4h). For this case study, the moderate mechanical and thermal turbulence causes vertical mixing in the fog layer, which slightly increases the surface horizontal visibility (370 m).

At the supersite, the fog dissipates after sunrise under cloud free atmosphere above its top height. The SHF continues to increase (Fig. 4h) due to solar radiation. During this phase, the RLWP becomes negative (-11.39 g m^{-2}) when the CTH increases significantly, in spite of the increase of the LWP (maximum of 43.34 g m^{-2}), while $\alpha_{eq}^{closure}$ remains around 0.63. Based on the RLWP, the fog conceptual model would predict a deficit of liquid water in the fog layer one hour before the lifting of its base height (Fig. 4g). The fog dissipation phase is induced by the increase of the vertical mixing generated by the thermal and mechanical turbulence associated with TKE values larger than 0.4 m^2 s^{-2} (Fig. 4f). The fog dissipation phase is marked by the daytime atmospheric convection associated with significant SHF (22.02 W m^{-2}) generating thermal turbulence (σ_w^2 = 0.06 m^2 s^{-2}), which allows more vertical mixing and warming of the daytime atmospheric boundary layer.

https://doi.org/10.5194/egusphere-2023-1224
Preprint. Discussion started: 9 June 2023

In summary, for this fog event, the fog conceptual model is consistent with the in-situ measurements of turbulence on the timing of the different fog phases. It has provided additional elements for understanding the different phases of the fog life cycle.

3.2 Case study 2 (IOP 6) analysis

Radar reflectivity time-cross sections derived from BASTA cloud radar during case study 2 (IOP 6) on the 5-6 January 2019 indicate that clear weather precedes fog formation at 20:40 UTC on 5 January 2020 (Fig. 5a and 5b). Fog develops below the dry, warm and cloud free stable atmospheric boundary layer (Fig. 5c). This case presents a spatial variability of fog formation time. The fog lasts 12 h and completely dissipates around 08:40 UTC, on 6 January 2020 at the supersite (see Table 1), while it dissipates earlier at Noaillan at 04:30 UTC. At all sites in the studied area, cold atmospheric conditions prevailed during the whole episode (Fig. 5e). The surface wind speed is moderate (< 3 m s^{-1}) and quite homogeneous in the studied area (Fig. 5d and 5f). The wind direction changed several times during the fog's evolution.

As in case study 1, before fog formation, hourly vertical profiles of temperature from the MWR (Fig. 6a) indicate a double stratification of the low atmosphere under an easterly low-level jet (Fig. 6d). Near surface air temperature is negative (Fig. 5e) and indicates frozen surface. These conditions are associated with an anticyclonic system across central Europe (not shown). During the fog pre-onset phase, the mean cooling rate at the supersite is -0.7 °C h^{-1} (Table 2). The continued decrease in temperature combined with the negative surface SHF (-0.17 W m^{-2}), southerly very low wind (0.2 m s^{-1}) at near surface, very low vertical velocity variance (σ_w^2 < 0.003 m^2 s^{-2}) and low TKE (0.06 m^2 s^{-2}) reveal that atmospheric conditions favorable to fog formation are driven by surface radiative cooling (Table 1), leading to a thermally-stable surface layer as in case study 1. Again, the fog onset precedes by a few minutes the minimum of SHF.

The fog stable phase is observed from 20:40 UTC to 03:00 UTC (3 h 20 min duration) under cloud-free conditions above fog top height. It is characterized by a thin fog (71 m) under a very deep temperature inversion (Fig. 6c), and light varying wind (Fig. 6d). Negative values of the equivalent fog adiabaticity by closure (-0.69) associated with decrease in temperature (-0.13 °C h^{-1}) (Fig. 5e), very low mean LWP (1.66 g m^{-2}) (Fig. 6g), and low turbulence (TKE = 0.09 m^2 s^{-2} and σ_w^2 = 0.009 $m^2 s^{-2}$) are sufficient conditions to maintain a thermally stable, optically-thin fog (242 m of horizontal visibility), as in case study 1. The continued increase of TKE in the fog layer (Fig. 6f), and surface SHF (Fig. 6h) triggered the start of the transition phase, limiting the duration of the stable phase compared to case 1 (IOP 5).

https://doi.org/10.5194/egusphere-2023-1224
Preprint. Discussion started: 9 June 2023

For case study 2, the fog transition phase is observed from 00:00 UTC to 02:00 UTC (2 h of duration) at the supersite (Fig. 6a and 6b). Its characteristics are similar to those found in case study 1 but the LWP (7.18 g m^{-2}), RLWP (+3.55 g m^{-2}), cooling rate (-0.007 °C h^{-1}) are lower and the TKE (0.23 $m^2.s^{-1}$) and SHF (7.76 W m^{-2}) larger. As in case study 1, these turbulent conditions allow a vertical mixing of the fog layer indicating its transition towards adiabatic fog.

Fog adiabatic phase is observed from 02:00 UTC to 08:40 UTC at the supersite. The first period from 02:00 UTC to 05:00 UTC is marked by a $\alpha_{eq}^{closure}$ larger than 0.5 and a strong increase in temperature (+2 °C), LWP (42 g m^{-2}), and a positive RLWP until 04:30 UTC. The temperature inversion above the fog layer strengthened and its top height lowered. The TKE in the fog layer and the vertical velocity variance continue to increase (TKE > 0.2 $m^2 s^{-2}$ and σ_w^2 > 0.02 $m^2 s^{-2}$). The SHF oscillates around 10 W m^{-1}. These conditions are favorable for the deepening of the fog by vertical mixing (see Fig. 5a and 6b). The second period from 05:00 UTC to 08:40 UTC is characterized by the $\alpha_{eq}^{closure}$ lower than 0.5, a decrease in surface temperature, stable base and top height of the temperature inversion, a sharp decrease in LWP, fog top height and RLWP (oscillating around 0 g m^{-2}), while the horizontal visibility increases and then decreases again. The decrease in turbulence (TKE < 0.2 $m^2.s^{-2}$) is linked to the decrease in wind speed in the fog layer, while the vertical velocity variance remains significant (σ_w^2 > 0.02 $m^2 s^{-2}$) with positive SHF. During the second half of the adiabatic phase, the fog layer that contains less than 20 g m^{-2} liquid water is not very resilient to the significant turbulence, as shown by the very low RLWP values and rapidly changing horizontal visibility.

The decrease in LWP seems to be driven by a possible phase change (water droplet to snow droplets) of the water droplets inducing a cooling in the fog layer and an increase in horizontal visibility. The dissipation of the mechanical turbulence favors the lowering of the fog thickness. These processes seem to be linked to the formation of snowflakes in the fog layer with fall due to their gravity which is consistent with the visual observations of scientists operating at the supersite, who reported frost on the tethered balloon.

As in case study 1, at the supersite, fog dissipates in the morning at 08:40 UTC, around sunrise. The RLWP predicted the fog dissipation at 07:30 UTC, one hour fifteen minutes before its total dissipation time. The surface vertical velocity variance became larger than 0.04 $m^2 s^{-2}$ and the TKE in the fog layer higher than 0.4 $m^2 s^{-2}$, the $\alpha_{eq}^{closure}$ oscillated around 0.5. These atmospheric characteristics in the fog layer are linked to the increase in turbulence associated with the increase of the wind speed (Fig. 5d) and the SHF (Fig. 5h), both induced by the convective mixing due to

https://doi.org/10.5194/egusphere-2023-1224
Preprint. Discussion started: 9 June 2023

solar radiation. Therefore, as in case study 1, the dissipation of fog is driven by the turbulence associated with mechanical and thermal processes.

3.3 Case study 3 (IOP 11) analysis

Radar reflectivity cross-sections on the 8-9 February 2020 (IOP 11) (Fig. 7a and 7b) indicate that this fog event is characterized by an early formation of fog at 20:40 UTC. Fog formation is preceded by a short rain (8.36 mm at Moustey) period produced by a stratocumulus cloud (Fig. 7b). After the rain, the water vapor in the lowest atmosphere starts to condensate as an ultra-low stratus cloud due to radiative cooling. From fog formation time up to 03:00 UTC,the sky is clear above the fog at the supersite. These atmospheric conditions allow a radiative cooling which favors the stabilization of the surface layer. Figure 7c indicates a spatio-temporal variability of fog formation time during a period of strong decrease in near surface temperature (Fig. 7e) at the beginning of the night and relatively light westerly wind (Fig. 7f and 7d). The formation of the fog started from the West and spread toward the East, illustrating a West-East gradient of fog formation in line with the westerly wind blowing in the studied area. During fog evolution, there is a spatial heterogeneity of temperatures up to 4°C between Moustey (western and coldest site) and Noaillan (eastern and warmest site). On the other hand, the dissipation is fairly homogeneous at all the sites, consecutive to an increase in air temperature and wind speed, and a shift in the wind direction (south-south-east to south), except at Noaillan where fog dissipation occurs earlier as visibility and temperature are higher than at the other sites. The fog dissipates at 03:40 UTC when the low atmosphere becomes neutral or unstable and the maximum radar reflectivity decreases and jumps in height (Fig. 8b). Just after the fog dissipation time, high clouds appear around 10 000 m height, characterising the change in air mass by advection.

Figure 8c shows that for this case study, the temperature inversion forms after the formation of the ultra-low stratus associated with the advection of the westerly Atlantic flow near the ground (Fig. 8d). The westerly flow brings wet and mild air over land and contributes to reduce the surface radiative cooling. The temperature inversion formed at the same time as the base of the stratus touches the ground, justifying the classification of fog formation by advection-radiation processes (Ryznar, 1977).

The formation of the fog considerably modified the dynamics of the low-level atmosphere by slowing down the radiative cooling, thus creating a thin layer of temperature inversion around 250 m thick with a low intensity of about 3 °C. The fog stable phase is observed from 20:40 UTC

https://doi.org/10.5194/egusphere-2023-1224
Preprint. Discussion started: 9 June 2023

and 23:00 UTC at the supersite. It is characterized by a clear sky above the fog top, a decrease in surface temperature (Fig. 8e) associated with a cooling rate of -0.53 °C h^{-1}, negative $\alpha_{eq}^{closure}$ (-0.69), low LWP (6.1 g m^{-2}) (Fig. 8g), low turbulence (TKE = 0.06 m^2 s^{-2} and σ_w^2 = 0.002 m^2 s^{-2}), and negative SHF (-1.7 W m^{-2}). As in cases 1 and 2, these atmospheric characteristics allow to maintain thermally-stable conditions.

Figure 8a indicates that the transition stable/adiabatic fog was observed between 23:00 UTC and 02:30 UTC (03:30 duration). The vertical profiles of radar reflectivity in Fig. 7a are consistent with the temperature profiles on the fog stable/adiabatic transition time. The transition time corresponds with the increase in height and intensity of the radar reflectivity. The fog transition is observed when on average, the visibility is minimum at Charbonnière (185 m), with low and negative cooling rate (-0.08 °C h^{-1}), low and negative $\alpha_{eq}^{closure}$ (-0.21) which are associated a low LWP (12.74 g m^{-2}) and a RLWP reaching (+10 g m^{-2}) (Table 2 and Fig. 8g). These characteristics of the transition estimated by the fog conceptual model are not consistent with those found by Toledo et al., 2021, but agree with the vertical profiles of temperature from the MWR (Fig. 8a) and the increase in turbulence (TKE = 0.1 m^2 s^{-2} and σ_w^2 = 0.008 m^2 s^{-2}) and SHF (-0.21 W m^{-2}) in the fog layer (Fig. 8f) due to a brisk change in wind direction and speed (Fig. 8d). In summary, the transition is driven by mechanical turbulence.

The fog adiabatic phase is observed from 02:30 UTC to 03:40 UTC (1 h 10 min duration) at the supersite under clear sky above the fog top. It is characterized by a decrease of the temperature inversion top height , of the RLWP (3.45 g m^{-2}) and the SHF (-0.49 W m^{-2}), and an increase of the LWP (30.7 g m^{-2}), $\alpha_{eq}^{closure}$ (0.54), and cooling rate (0.81 °C h^{-1}), while turbulence is kept constant. The vertical wind shear in the fog top height (Fig. 8d) generates dynamical instability driving the vertical mixing that reduces the temperature inversion above the fog top (Fig. 8c) which promotes the vertical development of the fog layer.

A sustainable dissipation is observed at 03:40 UTC. Figure 8d indicates that the dissipation time is associated with an increase of the wind regime (8 m s^{-1}) from the southeast in the entire low-level atmospheric column attesting the arrival at the supersite of an advected air mass. This front carried a warm air mass which increased rapidly the near surface temperature (1.34 °C h^{-1}) and allowed a deepening of the fog layer (see Fig. 8c). Advected air mass warms the fog layer causing the evaporation of the fog water droplets and the lifting of the water vapor by the vertical mixing driven by turbulence (TKE = 0.42 m^2 s^{-2} and σ_w^2 = 0.07 m^2 s^{-2}). Thus, the combination between the decrease in RLWP (2.03 g m^{-2}) and SHF (-3.02 W m^{-2}), the increase in $\alpha_{eq}^{closure}$ (0.6), surface

https://doi.org/10.5194/egusphere-2023-1224
Preprint. Discussion started: 9 June 2023

temperature (coupling between surface and fog), and turbulence, and a brisk wind allows the mixing of fog layer with dry air above resulting to the evolution as a stratus . The fog dissipation phase is thus driven by the advection of warm air at the supersite.

3.4 Case study 4 (IOP 14) analysis

As in case study 3 (Fig 7a), the time-cross section of radar reflectivity in Figure 9a indicates that the water vapor in the lowest atmosphere started to condensate as an ultra-low stratus cloud, associated with a radiative cooling (IOP 14). Fog formed at the supersite at 21:20 UTC. A stratus with a base height above the fog top height arrived at around 00:30 UTC corresponding with the fog vertical extension up to 200 m a.g.l. This cloud is advected from the northwest of the region and is captured by Meteosat Second Generation (MSG2) (not shown). The first fog dissipation time is observed at 04:00 UTC. Figure 9b shows that middle-altitude clouds are also observed at the supersite at around 06:20 UTC. These intermittent clouds contribute to the sustainable dissipation of the fog at 07:00 UTC by the lifting of its base height. The maximum fog thickness of 300 m is observed at around 06:00 UTC. In Figure 8c, the time evolution of the visibility at the five sites shows that the ftime of fog formation shows a shift from west to east, such as in case study 3. Surface temperatures are contrasted between sites after fog formation and become similar at 04:00 UTC. From midnight to the fog dissipation time, the near surface wind is also the same at all the sites and blown southerly with intermittent pulses. For the analysis of the processes involved in the evolution of this case study, we consider its evolution until its first dissipation at 04:00 UTC.

At the supersite, the fog pre-onset phase is characterized by a radiative cooling favoring the formation of a temperature inversion (Fig. 10c), the occurrence of a westerly wind (Fig. 10d) transporting mild and wet air from the Atlantic Ocean. The vertical wind shear created by the increase in wind reduces the intensity of the temperature inversion linked to the radiative cooling (-0.48 °C h^{-1}) (Fig. 10a); negative and low SHF (-1.17 W m^{-2}); low turbulence (TKE = 0.06 $m^2 s^{-2}$ and σ_w^2 = 0.002 $m^2 s^{-2}$) and allows the condensation of water vapor in the very low layers driving the triggering of the ultra-low stratus being the fog. For this episode, the occurrence of middle and high clouds and the increase in wind at the supersite attests that the fog pre-onset phase is driven by the advection and radiative cooling as observed in case study 3.

Fog stable phase is observed at the supersite from 21:20 UTC to 23:30 UTC (2 h 10 min duration) under cloud-free conditions above the fog. It is characterized by a low surface horizontal visibility (230 m), a negative $\alpha_{eq}^{closure}$ (-0.46), a high cooling rate (-0.88 °C h^{-1}), a stable temperature

https://doi.org/10.5194/egusphere-2023-1224
Preprint. Discussion started: 9 June 2023

inversion with 210 m thickness, low LWP (11.34 g m^{-2}), negative SHF (-3.26 W m^{-2}) and low turbulence (TKE = 0.09 $m^2 s^{-2}$ and σ_w^2 = 0.012 $m^2 s^{-2}$) (see Table 2 and Fig. 10).

The transition between stable and adiabatic fog is observed from 23:30 UTC to 01:00 UTC (1 h 30 min duration) (see Table 2). As in the previous case studies, this phase is well characterized by the vertical profiles of temperature and radar reflectivity (Fig. 10a and 10b, respectively) as well as the rapid increase of $\alpha_{eq}^{closure}$ (from -1.0 to +0.5), a positive RLWP (+11.93 g m^{-2}) associated with increasing LWP (21.19 g m^{-2}), moderate turbulence (TKE = 0.19 $m^2 s^{-2}$; σ_w^2 = 0.03 $m^2 s^{-2}$), low and negative SHF (-1.52 W m^{-2}) and positive cooling rate (+0.12 °C h^{-1}) (Table 2). The fog thickness at that time is 209 m and the visibility 249 m. Therefore, the transition phase is driven by the mechanical turbulence produced by the brisk horizontal wind at the supersite (Fig. 10d). The vertical shear associated with the wind allows a vertical mixing in the fog layer contributing to reduce the temperature inversion. Note that the brisk wind is associated with the arrival of the stratus above the fog top height (Fig. 9a and 10b).

At the supersite, fog adiabatic phase is observed from 00:20 UTC to 04:00 UTC (03:40 duration) during this case study. This phase includes a partial dissipation of the fog from 04:00 to 05:30 UTC. The first part of this phase is marked by an increase of the surface horizontal visibility (372 m), the deepening of the fog layer (CTH = 292 m) and the arrival of an advected stratus cloud. This period is characterized by episodic brisk winds of southerly flow (Fig. 9d). These episodic brisk winds are associated with intermittent turbulence (TKE = 0.22 $m^2 s^{-2}$ and σ_w^2 = 0.03 $m^2 s^{-2}$), weak temperature inversion, warming of surface layer (positive cooling rate (+0.47 °C h^{-1})), weak positive SHF (1.2 W m^{-2}), positive RLWP (+8.10 g m^{-2}), and high LWP (43.02 g m^{-2}). These characteristics allow the fog to remain optically thick (see Table 2), as in case study 1 and 2.

As in case study 3, the partial nocturnal dissipation of the fog is observed at 04:00 UTC for this episode. It is characterized by a negative cooling rate (-0.14 °C h^{-1}), a slight decrease in LWP (39.74 g m^{-2}) and SHF (0.82 W m^{-2}), negative RLWP (-2.32 g m^{-2}), moderate turbulence (TKE = 0.27 $m^{-2} s^{-2}$ and σ_w^2 > 0.04 $m^2 s^{-2}$), $\alpha_{eq}^{closure}$ = +0.6, and brisk wind at the supersite (Fig. 10d). This brisk wind is associated with an increase of the turbulence in the upper levels of the fog layer due to wind shear. The RLWP indicates that the fog conceptual model estimates fog dissipation time at 04:00 UTC (Fig. 10a) which is consistent with the horizontal visibility (more than 1000 m) and the maximum value of $\alpha_{eq}^{closure}$. These characteristics indicate that the first fog dissipation processes are driven by an advection of southern flow at the supersite, as in case study 3.

https://doi.org/10.5194/egusphere-2023-1224
Preprint. Discussion started: 9 June 2023

4. Discussion

Figure 11 shows for each fog phase, the mean vertical profiles of air temperature from the MWR and radar reflectivity from the cloud radar. It highlights the thermal characteristics of fog phases and differences in atmospheric conditions between fog categories: radiation and radiation-advection fogs.

For radiation fog case studies (1 and 2), the atmospheric conditions preceding (two hours before) fog formation are dominated by a strong and thick temperature inversion (more than 14 °C and 1000 m) which is associated with anticyclonic conditions over Europe favoring easterly wind and clear sky across the studied area. These atmospheric conditions allow a strong surface radiative cooling, negative heat fluxes and cooling of near surface air at a rate of -0.9 and -0.7 °C h^{-1} for case study 1 and 2, respectively. This cooling is associated with low turbulence indicated by low values of TKE (0.18 m^2 s^{-2} in case 1, and 0.06 in case 2) and near surface vertical velocity variance ($\sigma_w^2 <$ 0.003 m^2 s^{-2}) which reinforce the surface thermally stable boundary layer (Fig. 11a and 11b) favoring the triggering of radiation fog. These results are consistent with the definition of radiation fog proposed by Price, 2019.

In advection-radiation fog case studies (3 and 4), two hours before fog formation, a westerly sea breeze is present, transporting mild wet air from the ocean. Surface heat fluxes are negative, favoring cooling of the near-surface air (-1 °C h^{-1} in case study 3 and -0.5 °C h^{-1} in case study 4) and turbulent mixing is low (TKE < 0.06 m^2 s^{-2}). An East-West gradient of formation and dissipation is observed in line with the westerly synoptic advection of Atlantic inflow. Fog forms earlier in the West and dissipates later in the East. The combination of advection and radiative cooling favors fog formation at about 150 m a.g.l as an ultra-low stratus cloud followed by a rapid (less than 30 min) lowering of the stratus to the surface triggering the onset of the fog in an unstable (case 3) and neutral (case 4) surface atmospheric boundary layer (Fig. 11c and 11d).

The stable phase is characterized by a stable temperature profile and radar reflectivity which is maximum near the surface and decreases with height (see Fig. 11). The fog remains shallow (less than 100 m) with a low LWP ranging less than 12 g m^{-2} proportional to fog depth (Table 2). The equivalent fog adiabaticity by closure parameter ($\alpha_{eq}^{closure}$) is typically negative during the stable phase indicating that the fog is not in an adiabatic phase. The near-surface temperature decreases very moderately (-0.2 °C h^{-1}) in cases 1 and 2, while the air keeps cooling at about -1 °C h^{-1} in cases 3 and 4. For the four cases, surface heat fluxes are slightly negative (-3 to 0 W m^{-2}) and turbulence remains low (TKE at about 0.1 m^2 s^{-2} and σ_w^2 at 0.01 m^2 s^{-2}). This phase is characterized by very low

https://doi.org/10.5194/egusphere-2023-1224
Preprint. Discussion started: 9 June 2023

LWPs (1-2 g m^{-2} for radiation fogs and 6-11 g m^{-2} for advection-radiation fog). For radiation fog cases, the stable phase lasts around 6 and 4 hours, respectively, while for advection-radiation cases, it lasts around 2 hours. This is consistent with the strength of the surface inversion of each category of fog, as shown in Figure 10. These macrophysical characteristics of the fog stable phase are consistent with those found by Toledo et al., 2021.

The transition from stable to adiabatic phases is a key period in the fog life cycle. This period is well characterized using the macrophysical parameters of the conceptual model, namely the equivalent fog adiabaticity by closure ($\alpha_{eq}^{closure}$) parameter of the fog, the fog geometry (CTH) and fog LWP. During the transition from stable to adiabatic phases, these three parameters increase significantly (see Table 2). In particular, $\alpha_{eq}^{closure}$ evolves progressively from negative values towards +0.5 (Toledo et al., 2021). The transition phase lasts from 01:30 to 03:30, however its timing of occurrence is unpredictable (case 1 at (05:00 - 07:00 UTC), case 2 (00:00 - 02:00 UTC), case 3 (23:00 - 02:30 UTC), and case 4 (23:30 - 01:00 UTC). During this phase, a change is observed in static stability from stable profiles to neutral and adiabatic profiles (Fig. 11), while the radar reflectivity profile presents maximum values near the ground that decrease with height (Fig. 11). In cases 1, 2 and 4, the transition phase is characterized by an increase in turbulence that can explain the decrease in thermal stability of the fog layer, either shown in the vertical velocity variance (σ_w^2 >= 0.02 $m^2 s^{-2}$) associated with positive surface heat fluxes (cases 1 and 2), or TKE exceeding 0.3 $m^2 s^{-2}$. (cases 2 and 4). In all the cases, the fog LWP increases significantly which allows a more efficient radiative cooling of the fog layer, hence contributing to the destabilization of the fog layer. In case 3, the transition phase is not marked by a significant increase in turbulence. The transition is more progressive than in the other case studies (this phase lasts 03:30), the CTH is only 25 m deeper on average than during the stable phase, the $\alpha_{eq}^{closure}$ remains low during that phase, and reaches 0.5 at the end of the transition phase.

According to temperature vertical profiles from the MWR, at the end of the transition time from stable to adiabatic fog, the temperature profile becomes neutral or slightly unstable. This is consistent with the definition of the transition given by Price et al., 2011. We also find that it is during this period that the fog reaches its maximum value of RLWP, showing that the LWP increases beyond the critical liquid water path value, which gives information on the persistence of fog.

For radiation fog case studies, the adiabatic phase lasts 04:00 and 06:40 for case 1 and 2 respectively, maintaining the fog life cycle during the night until after sunrise. In cases 3 and 4, the

https://doi.org/10.5194/egusphere-2023-1224
Preprint. Discussion started: 9 June 2023

adiabatic phase is shorter and lasts 01:00 and 03:40, respectively, with a night-time dissipation at 03:40 and 04:00 UTC, respectively. In this fog phase, for radiation fog, the LWP ranges from 22-26 g m^{-2} with CTH near 190 m a.g.l. The fog is deeper for advection-radiation fog cases with LWP / CTH at 30 g m^{-2} / 200 m a.g.l and 43 g m^{-2} / 290 m a.g.l, respectively (Table 2). The adiabatic phase is characterized by an equivalent fog adiabatic by closure parameter near or above 0.5, and a positive but low RLWP. For all the cases except case 3, the adiabatic phase is associated with moderate turbulence in the fog layer (0.2 < TKE < 0.4 m^2 s^{-2} and 0.03 < σ_w^2 < 0.04 m^2 s^{-2}) which indicates significant vertical mixing generating an unstable surface atmospheric boundary layer (Fig. 11). This finding is consistent with the result of Ju et al., 2020 who based their analysis on one case study and Ghude et al., 2023, Dhangar et al., 2021 and Zhou and Ferrier, 2008 for more case studies analysis. In addition, this phase can also be driven by horizontal advection (mesoscale and synoptic systems) as in the case study 3.

This study shows two fog dissipation periods, at night and after sunrise. Daytime dissipation is observed for radiative fog cases and night-time dissipation for advection-radiation ones. All of them are observed when $\alpha_{eq}^{closure}$ > 0.5, TKE > 0.3 m^2 s^{-2}, σ_w^2 > 0.04 m^2 s^{-2}, and the LWP > 40 g m^{-2} (except case study 2). For cases 1 and 2, turbulence is thermally driven by positive SHF, while for cases 3 and 4, the night-time turbulence increase is mechanically driven by increased wind speed. For all cases, the RLWP decreases significantly from the stable phase to the dissipation phase, confirming that dissipation through fog-base lifting is linked to insufficient liquid water content in the fog layer, as suggested by the conceptual model. For case 3, the RLWP becomes negative 20 min after dissipation. This delay is likely due to very rapid changes in LWP and CTH at the time of dissipation.

5. Summary and Conclusions

The SOFOG3D field campaign provided a unique dataset documenting thermodynamic and dynamical atmospheric circulations to further understand the processes driving fog formation and dissipation over Southeastern France. Based on an innovative instrumental synergy combining in-situ and remote sensing measurements gathered in an adiabatic fog conceptual model, this study has documented the processes favoring fog evolution. The analysis has focused on four fog case studies: two radiative and two advective-radiative fogs. For each case study, we have defined the different phases characterizing the fog life cycle, namely (i) its formation, (ii) an initial phase where the fog develops under thermally stable conditions, (iii) a transition phase towards an adiabatic fog,

https://doi.org/10.5194/egusphere-2023-1224
Preprint. Discussion started: 9 June 2023

(iv) an adiabatic phase during which the fog vertical profile is adiabatic, and (v) a dissipation phase where the fog base lifts.

The results showed that for both radiation fog cases, the conditions are marked by very cold atmospheric conditions associated with a continental easterly nocturnal low-level jet. For these cases, the stable fog phase develops under weak turbulence and strong surface radiative cooling and strong and deep surface temperature inversion layer. The transition phase is driven by an increase in turbulence in the fog layer. This turbulence is associated with a change in the air mass thermodynamical characteristics by advection. The adiabatic phase is observed when the turbulence ($0.2 < TKE < 0.4$ m^2 s^{-2}) is sufficient to ensure vertical mixing in the fog layer. For these fog events, dissipation time is observed when the thermal and dynamic production of the turbulence are high ($TKE > 0.4$ m^2 s^{-1} and $\sigma_w^2 > 0.04$ m^2 s^{-2}). For this category of fog, the adiabatic fog conceptual model estimates the dissipation time one hour before its observation.

The analysis on the advection-radiation case studies shows that they have the shortest life cycle linked to the low surface boundary layer stability due to the vertical mixing generated by the westerly strong wind. In this category of fog, the processes driving the stable, stable/adiabatic transition and adiabatic phases are similar to those of the radiation fog category. However, the dissipation phase is driven by night-time horizontal advection at the supersite.

In summary, LWP and RLWP measured during SOFOG3D present lower values than at the SIRTA site, close to the uncertainty of the measurement. The conceptual model has therefore difficulties in integrating the mixing phases in the fog layer. Further development of the model is needed to adapt it to other regions before it can be used for nowcasting prediction. Fog formation, evolution and dissipation across southern France require an analysis of the synoptic atmospheric circulation in terms of wind, cloud cover, and thermodynamical processes. Indeed, this paper highlights that fog nowcasting in this region needs in addition to the numerical weather prediction models, a cloud radar, a microwave radiometer, a wind lidar, a surface energy balance, and meteorological stations. Operationalizing these instruments would allow to improve fog nowcasting, which will reduce its socioeconomic impacts in this region.

Appendix A: Fog conceptual model parametrization

A.1 Liquid water content

The conceptual model for adiabatic fog has been developed at SIRTA by Toledo et al., 2021. This model is a unidimensional model inspired by previous numerical models for stratus

https://doi.org/10.5194/egusphere-2023-1224
Preprint. Discussion started: 9 June 2023

clouds (Betts, 1982, Albrecht et al., 1990; and Cermak and Bendix, 2011) (see equation 1). The basic hypothesis is to consider a well-mixed fog layer and express the increase with height of the fog liquid water content as a function of the local adiabaticity ($\alpha(z)$) and the negative of the change in the saturation mixing ratio with height ($\Gamma_{ad}(T,P)$), given in equation A1.

$$\frac{dLWC(z)}{dz}=\alpha(z)\Gamma_{ad}(T,P) \qquad \text{(A1)}$$

Where T and P are air temperature and pressure, respectively. z is the height above the surface and varies between 0 and the cloud top height (CTH). By integrating equation 1, it is important to take into account fog geometry which is different from that of the stratus cloud. For a fog, the LWC at the base is non-zero due to the presence of liquid droplets down to the ground level. This presence of droplets drives surface visibility reduction and water deposition on the soil. Thus, as indicated in equation A2, the vertical integral of the LWC(z) is a function of the variation with height of the adiabaticity, $\Gamma_{ad}(T,P)$ and the measurement of the LWC at surface (LWC_0). This equation shows that the LWC increases with the thickness of the fog up to the height where upward motions of moisture from the surface are constrained by downward motions of dry air from the fog top height (Walker, 2003; Cermak and Bendix, 2011). From this interface level, the LWC decreases with height and becomes zero at the fog top height (Brown and Roach, 1976; Cermak and Bendix, 2011).

$$LWC(z)=\int_{z'=0}^{z'=z}\alpha(z')\Gamma_{ad}(T,P)\,dz'+LWC_0 \qquad \text{(A2)}$$

A.2 Liquid water path

The fog liquid water path (LWP) represents the total amount of liquid water present in the fog layer. It can be estimated by integrating equation A2 in height considering that the fog thickness is equivalent to the CTH (equation A3). An approximation assuming a constant adiabaticity is introduced by using the equivalent fog adiabaticity term $\alpha_{eq.}$ This simplifies the calculation, since a complete computation would require a knowledge of the vertical profile of adiabaticity which depends on the thermodynamic properties of the fog layer. In this conceptual model, the LWC is treated as if it increased linearly with height from the surface to the CTH. At the surface level the LWC from the model and fog are the same, connecting a given LWP with surface LWC. This quantity is converted to visibility values using Gultepe et al., 2006 parametrization. Hence, the

https://doi.org/10.5194/egusphere-2023-1224
Preprint. Discussion started: 9 June 2023

conceptual model connects fog LWP with its CTH and surface visibility values, it provides an estimation of the equivalent fog adiabaticity.

$$LWP = \frac{1}{2}\alpha_{eq}\Gamma_{ad}(T,P)CTH^2 + LWC_0 CTH \qquad \text{(A3)}$$

A.3 Critical liquid water path

Considering that the fog dissipates when its liquid water path is below a certain threshold depending on the local thermodynamic atmospheric conditions. In case of dissipation by lifting the base height of the fog, Wærsted, 2018 found a deficit in LWP in the fog layer. This assertion allows defining a minimum amount of LWP necessary to maintain the horizontal visibility at surface lower or equal to 1000 m, defined as the critical liquid water path (CLWP). Thus, based on equation A3, the CLWP can be expressed in equation A4 considering a critical liquid water content at surface (LWCc). Theoretically, the LWCc is the LWC that would cause a 1000 m visibility. It is estimated from the parameterization of Gultepe et al., 2006 based on the horizontal visibility at surface.

$$CLWP = \frac{1}{2}\alpha_{eq}\Gamma_{ad}(T,P)CTH^2 + LWC_c CTH \qquad \text{(A4)}$$

Data availability. All the data used in this study are hosted by the the French national center for Atmospheric data and services AERIS in the link https://sofog3d.aeris-data.fr/catalogue/#masthead. Data access can be free following the conditions fixed by the SOFOG3D project.

Competing interests. The authors claim no conflict of interest for this study.

Author contributions. **Cheikh DIONE:** Conceptualization, Methodology, Investigation, Validation, Formal-analysis, Writing – original draft, Writing – review & editing, Visualization. **Martial HAEFFELIN:** Supervision, Methodology, Investigation, Formal-analysis, Writing-original draft, Writing-review & Editing, , Funding acquisition. **Jean-Charles DUPONT:** Supervision, Investigation, Editing. **Felipe TOLEDO:** Methodology, Investigation, Editing. **Frederic BURNET:** Project administration, Resources, Investigation, Editing, Funding acquisition. **Christine LAC:** Supervision, resources, Investigation, editing, Funding acquisition. **Jean-Francois RIBAUD:** Visualization, Investigation, Editing. **Pauline MARTINET:** Editing, Investigation, Resources, Data curation. **Guylaine CANUT:** Investigation, Editing, Data curation. **Susana JORQUERA:** Data curation. **Julien DELANOË:** Data curation.

https://doi.org/10.5194/egusphere-2023-1224
Preprint. Discussion started: 9 June 2023

Acknowledgments. The SOFOG3D field campaign was supported by METEO-FRANCE and ANR through grant AAPG 2018-CE01-0004. Data are managed by the French national center for Atmospheric data and services AERIS. The CNRM/GMEI/LISA team supported the deployment, monitoring and data processing and supplying of Wind lidar and microwave radiometer.

References

1 Albrecht, B. A., Fairall, C. W., Thomson, D. W., White, A. B., Snider, J. B., and Schubert, W. H.: Surface-based remote sensing of the observed and the Adiabatic liquid water content of stratocumulus clouds, Geophys. Res. Lett., 17, 89-92, https://doi.org/10.1029/GL017i001p00089, 1990.

2 Bartok J, Bott A, Gera M.: Fog prediction for road traffic safety in a coastal desert region. Bound-Layer Meteor., 145(3), 485-506, https://doi.org/10.1007/s10546-012-9750-5, 2012.

3 Bartoková I, Bott A, Bartok J, Gera M.: Fog prediction for road traffic safety in a coastal desert region: Improvement of nowcasting skills by the machine-learning approach, Boundary-Layer. Meteor., 157, 501-516, https://doi.org/10.1007/s10546-015-0069-x, 2015.

4 Bell, A., Martinet, P., Caumont, O., Burnet, F., Delanoë, J., Jorquera, S., Seity, Y., and Unger, V.: An optimal estimation algorithm for the retrieval of fog and low cloud thermodynamic and micro-physical properties, Atmos. Meas. Tech., 15, 5415–5438, https://doi.org/10.5194/amt-15-5415-2022, 2022.

5 Bergot T.: Small-scale structure of journal radiation fog: a large-eddy simulation study, Q. J. R. Meteor. Soc., 139(673):1099-1112, https://doi.org/10.1002/qj.2051, 2013.

6 Bergot, T., Escobar, J. and Masson, V.: Effect of small-scale surface heterogeneities and buildings on radiation fog: Large-eddy simulation study at Paris-Charles de Gaulle Airport, Q. J. R. Meteor. S., 141(686), 285-298, https://doi.org/10.1002/qj.2358, 2015.

7 Betts, A. K.: Cloud Thermodynamic Models in Saturation Point Coordinates, J. Atmos. Sci., 39, 2182-2191, https://doi.org/10.1175/1520-0469(1982)039<2182:CTMISP>2.0.CO;2, 1982.

8 Boutle, I., Angevine, W., Bao, J.-W., Bergot, T., Bhattacharya, R., Bott, A., Ducongé, L., Forbes, R., Goecke, T., Grell, E., Hill, A., Igel, A.L., Kudzotsa, I., Lac, C., Maronga, B., Romakkaniemi, S., Schmidli, J., Schwenkel, J., Steeneveld, G.-J. and Vié, B.: Demistify: A large-eddy simulation (LES) and single-column model (SCM) intercomparison of radiation fog, Atmos. Chem. Phys., 22(1), 319-333, https://doi.org/10.5194/acp-22-319-2022, 2022.

9 Braun, R. A., Dadashazar, H., MacDonald, A. B., Crosbie, E., Jonsson, H. H., Woods, R. K., Flagan, R. C., Seinfeld, J. H., and Sorooshian, A.: Cloud Adiabaticity and Its Relationship to Marine

https://doi.org/10.5194/egusphere-2023-1224
Preprint. Discussion started: 9 June 2023

Stratocumulus Characteristics Over the Northeast Pacific Ocean, J. Geophys. Res. Atmos., 123, 13790-13806, https://doi.org/10.1029/2018JD029287, 2018.

10 Brown, R. and Roach, W.: The physics of radiation fog: II-a numerical study, Q. J. R. Meteor. Soc., 102, 335-354, https://doi.org/10.1002/qj.49710243205,1976.

11 Burnet, F.: SOFOG3D_TUZAN_CNRM_CEILOMETER-CL51-30SEC_L1. [Dataset], Aeris. https://doi.org/10.25326/241, 2021.

12 Canut, G.: SOFOG3D_CHARBONNIERE_CNRM_LIDARwindcube-TKE_L2. [Dataset]. Aeris. https://doi.org/10.25326/323, 2022.

13 Canut, G.: SOFOG3D_JACHERE_CNRM_TURB-30MIN_L2. [Dataset]. Aeris. https://doi.org/10.25326/91, 2020.

14 Canut, G.: SOFOG3D_JACHERE_CNRM_TURB-30MIN_L2. [Dataset], Aeris. https://doi.org/10.25326/91, 2020.

15 Cermak, J. and Bendix, J.: Detecting ground fog from space - a microphysics-based approach, Int. J. Remote Sens., 32, 3345-3371, https://doi.org/10.1080/01431161003747505, 2011.

16 Crewell. S., and Löhnert, U.: Accuracy of cloud liquid water path from ground-based microwave radiometry 2. Sensor accuracy and synergy, Radio. Sci., 38(3), 8042, https://doi.org/10.1029/2002RS002634, 2003.

17 Delanoë, J., Protat, A., Vinson, J.-P., Brett, W., Caudoux, C., Bertrand, F., Du Chatelet, J. P., Hallali, R., Barthes, L., Haeffelin, M., et al.: BASTA: A 95-GHz FMCW Doppler Radar for Cloud and Fog Studies, J. Atmos. Ocean. Technol. 33, 10231038: https://doi.org/10.1175/JTECH-D-15-0104.1, 2016.

18 Dhangar, N.G., Lal, D.M., Ghude, S.D. et al.: On the Conditions for Onset and Development of Fog Over New Delhi: An Observational Study from the WiFEX, *Pure Appl. Geophys.* 178, 3727-3746, https://doi.org/10.1007/s00024-021-02800-4, 2021.

19 Dias Neto, J., Nuijens, L., Unal, C., and Knoop, S.: Combined wind lidar and cloud radar for high-resolution wind profiling, Earth Syst. Sci. Data, 15, 769-789, https://doi.org/10.5194/essd-15-769-2023, 2023.

20 Ducongé, L., C. Lac, B. Vié, T. Bergot, and J. D., Price, Fog in heterogeneous environments : The relative importance of local and non local processes on radiative advective fog formation, *Q. J. R. Meteor. Soc.*, *146*, 2522-2546, https://doi.org/10.1002/qj.3783, 2020.

21 Dupont, J.-C., Haeffelin, M., Protat, A., Bouniol, D., Boyouk, N., and Morille, Y.: Stratus-fog formation and dissipation: a 6-day case study, Bound.-Layer. Meteorol., 143, 207-225, https://doi.org/10.1007/s10546-012-9699-4, 2012.

22 Fathalli, M., Lac, C., Burnet, F., Vié B.: Formation of fog due to stratus lowering: An observational and modeling case study, Q. J. R. Meteor. Soc., https://doi.org/10.1002/qj.4304, 2022.

23 Fernando, H. J., Gultepe, I., Dorman, C., Pardyjak, E., Wang, Q., Hoch, S. W., et al.: C-FOG: life of coastal fog, Bull Am Meteor Soc 102(2):E244–E272. https://doi.org/10.1175/BAMS-D-19-0070.1, 2021.

24 Foken, T., Göckede, M., Mauder, M., Mahrt, L., Amiro, B. D., and Munger, J. W.: Post-field data quality control, in: Handbook of Micrometeorology: A Guide for Surface Flux Measurement and Analysis, edited by: Lee, X., Massman, W. J., and Law, B., Kluwer, Dordrecht, 181-208, https://doi.org/10.1007/1-4020-2265-4, 2004.

25 Ghude, S. D., et al.: WiFEX: Walk into the warm fog over Indo Gangetic Plain region. Bulletin of the American Meteorological Society., https://doi.org/10.1175/BAMS-D-21-0197.1, 2023.

26 Huang, H. B., Chen, C. Y.: Climatological aspects of dense fog at Urumqi Diwopu International Airport and its impacts on flight on-time performance. Nat Hazards 81(2):1091-1106, https://doi.org/10.1007/s11069-015-2121-z, 2016.

27 Haeffelin, M., Bergot, T., Elias, T., Tardif, R., Carrer, D., Chazette, P., Colomb, M., Drobinski, P., Dupont, E., Dupont, J.-C., Gomes, L., Musson-Genon, L., Pietras, C., Plana-Fattori, A., Protat, A., Rangognio, J., Raut, J.-C., Rmy, S., Richard, D., Sciare, J. and Zhang, X.: Parisfog: shedding new light on fog physical processes. Bulletin of the American Meteorological Society., 91(6), 767-783, https://doi.org/10.1175/2009BAMS2671.1, 2010.

28 Koračin, D., Dorman, C. E., Lewis, J. M., Hudson, J. G., Wilcox, E. M., Torregrosa A.: Marine fog: a review, Atmos. Res., 143:142-175, https://doi.org/10.1016/j.atmosres.2013.12.012, 2014.

29 Kumer, V. M., Reuder, J., Dorninger, M., Zauner, R., Grubišić, V.: Turbulent kinetic energy estimates from profiling wind LiDAR measurements and their potential for wind energy applications, Renew Energy., 99, 898-910, https://doi.org/10.1016/j.renene.2016.07.014, 2016.

30 Liao, H., Jing, H., Ma, C., Tao, Q., Li, Z.: Field measurement study on turbulence field by wind tower and Windcube Lidar in mountain valley, Journal of Wind Engineering and Industrial Aerodynamics., 197, 104090, ISSN 0167-6105, https://doi.org/10.1016/j.jweia.2019.104090, 2020.

31 Liu, D. Y., Niu S. J., Yang, J., Zhao, L. J., Lü, J. J., Lu, C. S.: Summary of a 4-year fog field study in northern Nanjing, Part 1: fog boundary layer, Pure. Appl. Geophys., 169(5-6), 809-819, https://doi.org/10.1007/s00024-011-0343-x, 2012.

32 Liu, D. Y., Yan, W. L., Yang, J., Pu, M. J., Niu, S. J., Li, Z. H.: A study of the physical processes of an advection fog boundary layer, Boundary- Layer. Meteor., 158, 125-138, https://doi.org/10.1007/s10546-015-0076-y, 2016.

33 Maalick, Z., Kühn, T., Korhonen, H., Kokkola, H., Laaksonen, A. and Romakkaniemi, S.: Effect of aerosol concentration and absorbing aerosol on the radiation fog life cycle, Atmospheric Environment, 133, 26-33, https://doi.org/10.1016/j.atmosenv.2016.03.018, 2016.

34 Marke, T., Ebell, K., Löhnert, U., Turner, D. D.: Statistical retrieval of thin liquid cloud microphysical properties using ground-based infrared and microwave observations, J. Geophys. Res. Atmos., 121(24):14-558, https://doi.org/10.1002/2016JD025667, 2016.

35 Martinet, P., Unger, V., Burnet, F. *et al.:* A dataset of temperature, humidity, and liquid water path retrievals from a network of ground-based microwave radiometers dedicated to fog investigation, *Bull. of Atmos. Sci. Technol.,* **3**, 6, https://doi.org/10.1007/s42865-022-00049-w, 2022.

36 Martinet, P. (2021). SOFOG3D_CHARBONNIERE_CNRM_MWR-HATPRO-LWP_L2. [Dataset]. Aeris. https://doi.org/10.25326/207

37 Mauder, M., Cuntz, M., Drüe, C., Graf, A., Rebmann, C., Schmid, H. P., Schmidt, M., and Steinbrecher, R.: A strategy for quality and uncertainty assessment of long-term eddy-covariance measurements, Agr. Forest Meteorol., 169, 122-135, https://doi.org/10.1016/j.agrformet.2012.09.006, 2013.

38 Mazoyer, M., Lac, C., Thouron, O., Bergot, T., Masson, V., and Musson-Genon, L.: Large eddy simulation of radiation fog: impact of dynamics on the fog life cycle, *Atmos. Chem. Phys.*, *17*, 13017-13035, https://doi.org/10.5194/acp-17-13017-2017, 2017.

39 Nakanishi M.: Large-Eddy simulation of radiation fog, Bound-Layer Meteor., 94, 461-493, https://doi.org/10.1023/A:1002490423389, 2000.

40 Niu, S., Lu , C., Yu , H., Zhao, L., and Lü, L.: Fog research in China: an overview, Adv. Atmos. Sci., 27(3), 639-662, https://doi.org/10.1007/s00376-009-8174-8, 2010a.

41 Niu, S., Lu , C., Zhao , J., Lu, J, and Yang , J.: Analysis of the microphysical structure of heavy fog using a droplet spectrometer: a case study, Adv. Atmos. Sci., 27(6), 1259-1275, https://doi.org/10.1007/s00376-010-8192-6, 2010b.

42 Pauli, E., Cermak, J., Andersen, H.: A satellite-based climatology of fog and low stratus formation and dissipation times in central Europe, Q. J. Roy. Meteorol. Soc., 148, 1439-1454, https://doi.org/10.1002/qj.4272, 2022.

43 Philip, A., Bergot, T., Bouteloup, Y., and Bouyssel, F.: The impact of vertical resolution on fog forecasting in the kilometric-scale model Arome: a case study and statistics, Weather Forecast., 31, 1655-1671, https://doi.org/10.1175/WAF-D-16-0074.1, 2016.

44 Pithani, P., Ghude, S.D., Jenamani, RK., Biswas, M., Naidu, C.V., Debnath, S., Kulkarni, R., Dhangar, N.G., Jena, C., Hazra, A., Phani, R., Mukhopadhyay, P., Prabhakaran, T., Nanjundiah, R.S., Rajeevan, M.: Real-time Forecast Of Dense Fog Events Over Delhi: The Performance Of the WRF Model During WiFEX Field Campaign. Weather and Forecasting, 35(2), 739-756, https://doi.org/10.1175/waf-d-19-0104.1, 2020.

45 Price, J. D.: On the formation and development of radiation fog: an observational study. Bound-Layer Meteor., 172, 167-197, https://doi.org/10.1007/s10546-019-00444-5, 2019.

https://doi.org/10.5194/egusphere-2023-1224
Preprint. Discussion started: 9 June 2023

46 Price, J. D., Lane, S., Boutle, I. A., Smith, D. K. E., Bergot, T., Lac, C., Duconge, L., McGregor, J., Kerr-Munslow, A., Pickering, M., and Clark, R.: LANFEX: a field and modeling study to improve our understanding and forecasting of radiation fog, *Bull. Amer. Meteo. Soc.*, *99*, 2061-2077, https://doi.org/10.1175/BAMS-D-16-0299.1, 2018.

47 Price, J.: Radiation Fog. Part I: Observations of Stability and Drop Size Distributions, Boundary-Layer Meteorol., 139, 167-191, https://doi.org/10.1007/s10546-010-9580-2, 2011.

48 Price, J., Porson, A., and Lock, A.: An observational case study of persistent fog and comparison with an ensemble forecast model, Boundary-Layer. Meteorol., 155, 301-327, https://doi.org/10.1007/s10546-014-9995-2, 2015.

49 Roach, W.: Back to basics: Fog: Part 2 - the formation and dissipation of land fog, Weather., 50(1), 7-11, 1995.

50 Román-Cascón, C., Steeneveld, G. J., Yagüe, C., Sastre, M., Arrillaga, J. A., and Maqueda, G.: Forecasting radiation fog at climatologically contrasting sites: Evaluation of statistical methods and WRF. Q. J. R. Meteorol. Soc., 142(695), 1048-1063, https://doi.org/10.1002/qj.2708, 2016.

51 Ryznar, E.: Advection-radiation fog near Lake Michigan, Atmos. Environ. 11, 427-430, https://doi.org/10.1016/0004-6981(77)90004-X, 1977.

52 Steeneveld, G. J., Ronda, R. J., and Holtslag, A. A. M.: The challenge of forecasting the onset and development of radiation fog using mesoscale atmospheric models, Boundary-Layer Meteorology, 154(2), 265-289, https://doi.org/10.1007/s10546-014-9973-8, 2015.

53 Tardif, R. and Rasmussen, R. M.: Event-based climatology and typology of fog in the New York City region, J. Appl. Meteorol. Clim., 46, 1141-1168, https://doi.org/10.1175/JAM2516.1, 2007.

54 Ju, T., Wu, B., Zhang, H., Liu, J., 2020.: Characteristics of turbulence and dissipation mechanism in a polluted advection-radiation fog life cycle in Tianjin, Meteorology and Atmospheric Physics., https://doi.org/10.1007/s00703-020-00764-z, 2020.

55 Toledo, F., Haeffelin, M., Wærsted, E., and Dupont, J.-C.: A new conceptual model for adiabatic fog, Atmos. Chem. Phys., 21, 13099–13117, https://doi.org/10.5194/acp-21-13099-2021, 2021.

56 Felipe Toledo Bittner. Improvement of cloud radar products for fog surveillance networks : fog life cycle analyses and calibration methodologies, Ph.D. Thesis, Institut Polytechnique de Paris, France, ⟨NNT : 2021IPPAX029⟩. ⟨tel-03298445⟩, 2021.

57 Toledo, F., Delanoë, J., Haeffelin, M., Dupont, J.-C., Jorquera, S., and Le Gac, C.: Absolute calibration method for frequency-modulated continuous wave (FMCW) cloud radars based on corner reflectors, Atmos. Meas. Tech., 13, 6853-6875, https://doi.org/10.5194/amt-13-6853-2020, 2020.

58 Wærsted, E. G., Haeffelin, M., Steeneveld, G.-J., and Dupont, J.-C.: Understanding the dissipation of continental fog by analysing the LWP budget using idealized LES and in situ observations, Q. J. Roy. Meteor. Soc., 145, 784-804, https://doi.org/10.1002/qj.3465, 2019.

59 Wærsted, E. G. Description of physical processes driving the life cycle of radiation fog and fog-stratus transitions based on conceptual models, Ph.D. Thesis, Paris Saclay, 2018.

60 Wærsted, E. G., Haeffelin, M., Dupont, J.-C., Delanoë, J., and Dubuisson, P.: Radiation in fog: quantification of the impact on fog liquid water based on ground-based remote sensing, Atmos. Chem. Phys., 17, 10811–10835, https://doi.org/10.5194/acp-17-10811-2017, 2017.

61 Walker, M.: The science of weather: Radiation fog and steam fog, Weather, 58, 196-197, https://doi.org/10.1256/wea.49.02, 2003.

62 Zhou, B., and Ferrier, B. S.: Asymptotic analysis of equilibrium in radiation fog. Journal of Applied Meteorology and Climatology, 47, 1704-1722. https://doi.org/10.1175/2007JAMC1685.1, 2008.

https://doi.org/10.5194/egusphere-2023-1224
Preprint. Discussion started: 9 June 2023

List of tables

Table 1 : Case study number, fog onsets, type of fog formation, fog dissipation times, fog duration and type of fog dissipation for the four documented case studies. Time is in UTC. Dates are in the format “dd/mm/yyyy”. “dd” indicates the day, “mm” the month, and “yyyy” the year.

Table 2 : Summary of fog features at the supersite during the five defined phases during its evolution for each case study. The formation, dissipation times are estimated using the visibility (m) from the Scatterometer. The transition from stable to adiabatic fog is defined using temperature from the microwave radiometer. The cooling rate (dT/dt), wind speed (WS), and wind direction (WD) are derived from the meteorological station. Sensible heat flux (SHF), turbulent kinetic energy (TKE) and the vertical velocity variance (σ_w^2) at 3 m a.g.l are derived from the flux station. The liquid water path (LWP) is estimated from the MWR. The fog reservoir of liquid weather path (RLWP) and the equivalent adiabaticity of closure $\alpha_{eq}^{closure}$ parameter are computed by the conceptual model. Fog top height (FTH) and middle and high cloud base and top heights are derived from the radar reflectivity from Basta cloud radar.”-” indicates that the variables are not measurable or calculable.

https://doi.org/10.5194/egusphere-2023-1224
Preprint. Discussion started: 9 June 2023

List of figures

Figure 1: In a), the geographical map of the study area of the SOFOG3D field campaign including the five instrumented sites (Agen, Bergerac, Biscarrosse, Mont-de-Marsan, and Saint-Symphorien) where a microwave radiometer was installed. Blue lines indicate the rivers. The cities are indicated in black dots. The most instrumented domain around the supersite is indicated in a) by the red rectangle. In b), the orography of a 100 x 100 km^2 domain centered on Charbonnière which includes locations of four of the meteorological stations installed around the supersite used in this study. Orography data are from the National Aeronautics and Spatial Administration (NASA) shuttle radar topography mission (SRTM) (90 m of resolution).

Figure 2: Figure 2: (a) Scatter plot of the equivalent adiabaticity by closure versus the CTH and LWP at the supersite. b) Boxplot of the equivalent adiabaticity by closure versus the different LWP ranges from the MWR. In b), numbers at the figure top indicate total values included in each boxplot and computed between 2 hours before and after the fog. Horizontal dashed line indicates the threshold of the equivalent adiabaticity from closure defining the transition from stable to adiabatic fog.

Figure 3: In (a-b) time-height cross-section from surface up to 600 and 12000 m, respectively of radar reflectivity from Basta (shaded) radar, time evolution of the cloud top height from Basta (red line), and the cloud base height from the Celiometer (CL51) (green line). Time evolution of (c) surface visibility, (d) 10 m wind speed, (e) 2 m air temperature, and (f) 10 m wind direction observed on the 28-29 December 2019 (case study 1, IOP 5) at the five meteorological stations (in red, black, blue, green, and pink lines for Moustey (1 m a.g.l), Charbonnière (3 m a.g.l), Cape Sud (3 m a.g.l), Tuzan (3 m a.g.l), and Noaillan (1 m a.g.l), respectively) deployed around the supersite. Note that wind was not collected at Tuzan. In (c), the visibility measured at Moustey was interrupted by technical issues. Vertical black dashed lines indicate fog formation (left) and dissipation (right) times. Green dashed lines show the transition time from stable fog to adiabatic fog (fog mature phase). Red dashed line indicates the sunrise.

Figure 4: Evolution of fog macrophysical characteristics observed on the 28-29 December 2019 (case study 1, IOP 5) at Charbonnière. In (a-b) vertical profiles of air temperature from the Hatpro microwave radiometer (MWR) and radar reflectivity from Basta radar, respectively. In (c) time-

https://doi.org/10.5194/egusphere-2023-1224
Preprint. Discussion started: 9 June 2023

height cross-section of air temperature from the MWR (shaded), time evolution of inversion top height (ITH) (open gray circles), inversion base height (IBH) (open gray squares), cloud top height (CTH) from the cloud radar (open black squares), and the cloud base height (CBH) from the Celiometer (open black circles). In (d) wind speed (shaded) and direction (arrows) from the WindCube. Arrows in (d) indicate only the direction of the horizontal flow. Time evolution of (e) air temperature at 3 m a.g.l from the meteorological station (red line) and equivalent adiabaticity of closure from the fog conceptual model (blue line), (f) the mean of the turbulent kinetic energy (TKE) in the layer 40 – 220 m for the WindCube (black line) and the TKE (blue line) and vertical velocity variance (red line) at 3 m a.g.l from the flux station at Charbonnière, (g) the LWP estimate from the MWR (blue line), the RLWP from the fog conceptual model (red line), and (h) sensible heat fluxes (SHF) (red and blue lines, respectively) from the flux station. Vertical black dashed lines indicate fog formation and dissipation times. Green dashed lines indicate the transition period (fog mature phase) from stable to adiabatic fog. The red dashed line indicates sunrise.

Figure 5: As in Figure 3 but for the 5-6 January 2020 (case study 2, IOP 6). In (c), only Charbonnière and Noaillan have valid data. In (c), the visibility measured at Moustey, Tuzan and Cape Sud were interrupted by technical issues.

Figure 6: As in Figure 4 but for the 5-6 January 2020 (case study 2, IOP6).

Figure 7: As in Figure 3 but for the 8-9 February 2020 (case study 3, IOP 11).

Figure 8: As in Figure 4 but for the 8-9 February 2020 (case study 3, IOP 11).

Figure 9: As in Figure 3 but for the 7-8 March 2020 (case study 4, IOP 14).

Figure 10: As in Figure 4 but for the 7-8 March 2020 (case study 4, IOP 14). The LWP, RLWP, and $\alpha_{eq}^{closure}$ are disrupted between 00:30 and 02:30 UTC because the LWP estimated by the MWR take into account the liquid water in the advected stratus.

Figure 11: Vertical profiles of air temperature and radar reflectivity put together for each fog case study: (a) for case study 1, (b) case study 2, (c) case study 3 and (d) case study 4. Line and shaded

https://doi.org/10.5194/egusphere-2023-1224
Preprint. Discussion started: 9 June 2023

area indicate the mean and standard deviation of air temperature and radar reflectivity during each fog phase.

https://doi.org/10.5194/egusphere-2023-1224
Preprint. Discussion started: 9 June 2023

Table 2 : Summary of fog features at the supersite, during the five defined phases during it evolution for each case study. The formation, dissipation times are estimated using the visibility (m) from Scatterometer. The cooling rate (dT/dt), wind speed (WS) and wind direction (WD) are derived from the meteorological station. Sensible heat flux (SHF), turbulent kinetic energy (TKE), and the vertical velocity variance (σ_w^2) at 3 m a.g.l are derived from the flux station. The liquid water path (LWP) is estimated from the MWR. The fog reservoir of liquid weather path (RLWP) and the equivalent adiabaticity of closure $\alpha_{eq}^{closure}$ parameter are computed by the conceptual model. Fog top height (FTH) and middle and high cloud base and top heights are derived from the radar reflectivity from Basta cloud radar."-" indicates that the variables are not measurable or calculable.

Case study number	Phase names	Time range	Duration (h:min)	Visibility (m)	dT/dt (°C h^{-1})	$\alpha_{eq}^{closure}$ g m^{-3}	LWP (g m^{-2})	RLWP max (g m^{-2})	FTH (m a.g.l)	WS (m s^{-1})	WD (°)	TKE (m² s^{-2})	σ_w^2 (m² s^{-2})	SHF (W m^{-2})	Cloud above fog (m a.g.l)
	Pre-fog phase	[20:50 - 22:50]	2:00	9962	-0.9	-	0	-	-	0.61	61	0.18	0.002	-0.23	clear
	Stable	[22:50 - 05:00]	6:10	736	-0.18	-1.3	2.18	-	51	0.7	84	0.12	0.01	-1.16	clear
1 (IOP5)	Transition stable/adiabatic	[05:00 - 07:00]	2:00	173 – 262	0.08	-0.8 – 0.4	7 – 28	8 – 15	68 – 181	0.5 – 2.1	68 – 112	0.07 – 0.17	0.02 – 0.03	2.3 – 8.8	clear
	Adiabatic	[07:00 - 11:00]	4:00	370	0.77	0.5	26.16	6.38	185	2.4	116	0.28	0.04	12.9	[8000 - 10000]
	Dissipation	[10:30 - 11:30]	1:00	1549	1.1	0.63	43.34	-11.39	288	2.6	94	0.46	0.06	22.02	clear
	Pre-fog	[18:40 - 20:40]	2:00	15566	-0.7	-	0	-	-	0.2	195	0.06	0.003	-0.17	clear
	Stable	[20:40 - 00:00]	3:20	242	-0.13	-0.69	1.66	-	71	1	183	0.09	0.009	0.28	clear
2 (IOP6)	Transition stable/adiabatic	[00:00 - 02:00]	2:00	219 – 291	-0.007	-0.2 – 0.45	0.3 – 17	-0.23 – 3.8	81 – 168	1.6 – 2.6	149 – 147	0.35 – 0.25	0.02 – 0.04	3.7 – 11	clear
	Adiabatic	[02:00 - 08:40]	6:40	450	0.17	0.51	22.14	1.51	191	2.2	110	0.27	0.04	6.62	clear
	Dissipation	[08:10 - 09:10]	1:00	944	0.43	0.53	11.62	-7.63	187	2.5	136	0.33	0.048	14.02	[250 - 1000]
	Pre-fog	[18:40 - 20:40]	2:00	13239	-1.03	-	0	-	-	1.3	242	0.03	0.011	-5.5	rain
	Stable	[20:40 - 23:00]	2:20	243	-1.2	-0.69	6.10	-	77	1	220	0.06	0.002	-1.7	clear
3 (IOP11)	Transition stable/adiabatic	[23:00 - 02:30]	3:30	134 – 260	-0.08	-1.35 – 0.4	5 – 19.8	7.7 – 6	50 – 156	1.8 – 0.4	144 – 78	0.07 – 0.04	0.006 – 0.004	-1.9 – -0.2	clear
	Adiabatic	[02:30 - 03:40]	1:10	271	0.81	0.54	30.70	3.45	204	1	120	0.08	0.008	-0.49	clear
	Dissipation	[03:10 - 04:10]	1:00	1445	1.34	0.6	41.90	2.03	235	3.6	143	0.42	0.07	-3.02	clear
	Pre-fog	[19:20 - 21:20]	2:00	14088	-0.47	-	0	-	-	1.1	233	0.06	0.002	-1.17	[5000 - 6000] [8000 - 10000]
	Stable	[21:20 - 23:30]	2:10	230	-0.88	-0.46	11.34	-	81	1.2	177	0.09	0.012	-3.26	clear
4 (IOP14)	Transition stable/adiabatic	[23:30 - 01:00]	1:30	240 – 253	0.12	-0.17 – 0.64	10.9 – 59.2	10 – -	106 –209	1.6 – 2.7	141 – 184	0.08 – 0.32	0.01 – 0.05	-1.6 – 2.7	clear
	Adiabatic	[00:20 - 04:00]	3:40	372	0.47	0.59	43.02	8.10	292	2	179	0.22	0.03	1.2	[250 - 500]
	Dissipation	[03:30 - 04:30]	1:00	1160	-0.14	0.60	39.74	-2.32	240	2.7	174	0.27	0.04	0.82	clear

https://doi.org/10.5194/egusphere-2023-1224
Preprint. Discussion started: 9 June 2023

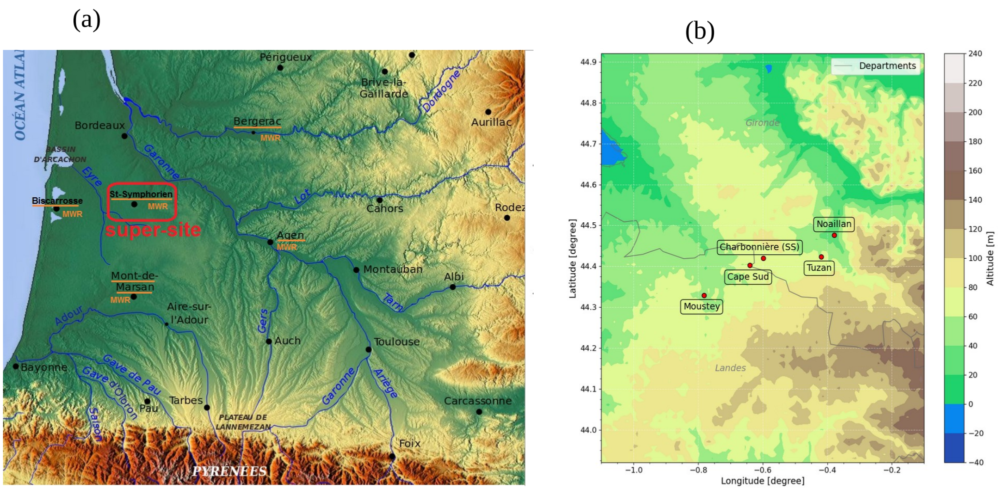

Figure 1 : In a), the orography of the study area of the SOFOG3D field campaign including the five instrumented sites (Agen, Bergerac, Biscarrosse, Mont-de-Marsan, and Saint-Symphorien) where a microwave radiometer was installed. Blue lines indicate the rivers. The cities are indicated in black dots. The most instrumented domain around the supersite is indicated in a) by the red rectangle. In b), the orography of a 100 x 100 km^2 domain centered on Charbonnière which includes locations of four of the meteorological stations installed around the supersite and used in this study. Orography data are from the National Aeronautics and Spatial Administration (NASA) shuttle radar topography mission (SRTM) (90 m of resolution).

https://doi.org/10.5194/egusphere-2023-1224
Preprint. Discussion started: 9 June 2023

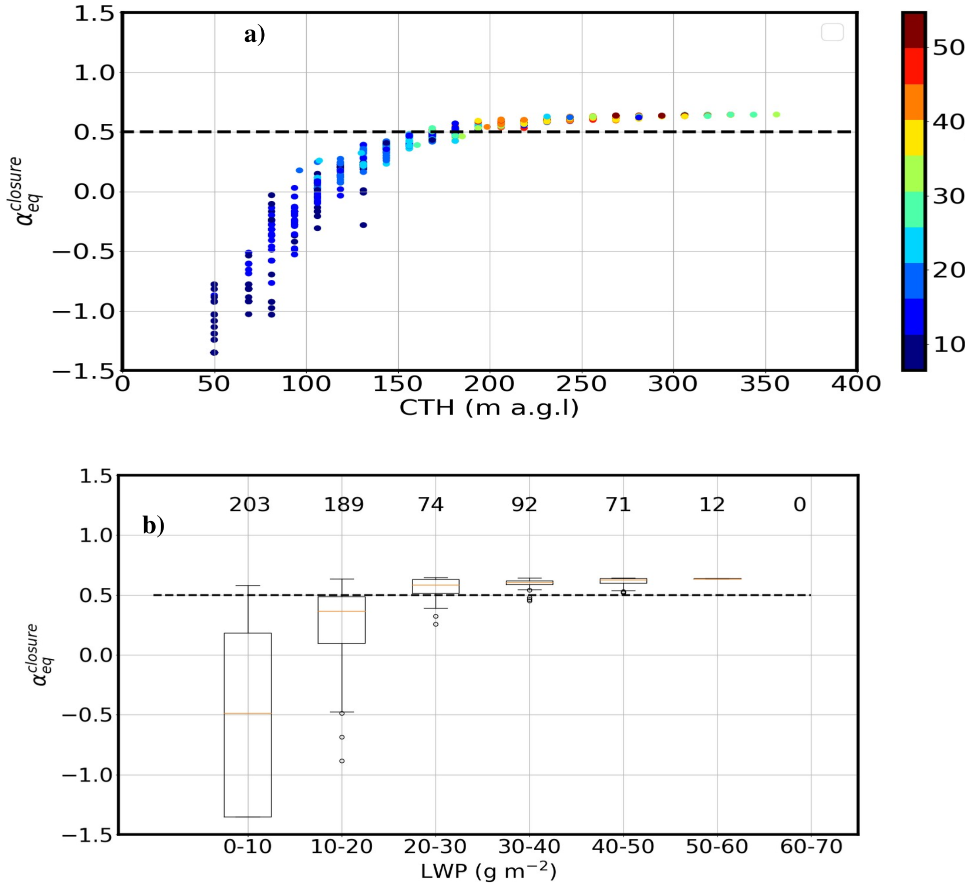

Figure 2: In (a) Scatter plot of the equivalent adiabaticity by closure versus the CTH and LWP (colored circles) at the supersite. b) Boxplot of the equivalent adiabaticity by closure versus the different LWP ranges from the MWR. In b), numbers at the figure top indicate total values included in each boxplot and computed between 2 hours before and after the fog. Horizontal dashed line indicates the threshold of the equivalent adiabaticity from closure defining the transition from stable to adiabatic fog.

https://doi.org/10.5194/egusphere-2023-1224
Preprint. Discussion started: 9 June 2023

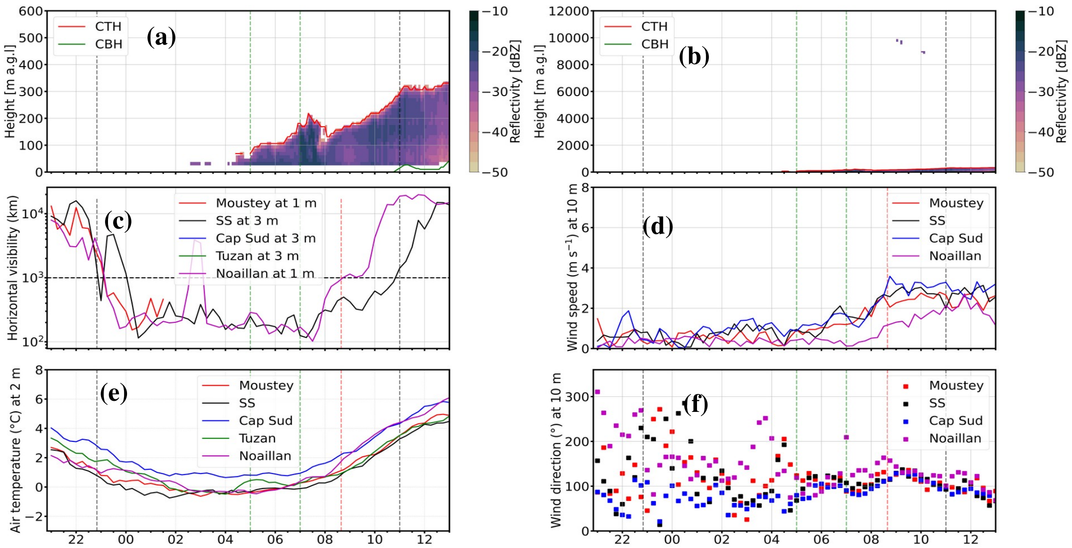

Figure 3: In (a-b) time-height cross-section from surface up to 600 and 12000 m, respectively of radar reflectivity from Basta (shaded) radar, time evolution of the cloud top height from Basta (red line), and the cloud base height from the Celiometer (CL51) (green line). Time evolution of (c) surface visibility, (d) 10 m wind speed, (e) 2 m air temperature, and (f) 10 m wind direction observed on the 28-29 December 2019 (case study 1, IOP 5) at the five meteorological stations (in red, black, blue, green, and pink lines for Moustey (1 m a.g.l), Charbonnière (3 m a.g.l), Cape Sud (3 m a.g.l), Tuzan (3 m a.g.l), and Noaillan (1 m a.g.l), respectively) deployed around the supersite. Note that wind was not collected at Tuzan. In (c), the visibility measured at Moustey was interrupted by technical issues. Vertical black dashed lines indicate fog formation (left) and dissipation (right) times. Green dashed lines show the transition time from stable fog to adiabatic fog (fog mature phase). Red dashed line indicates the sunrise.

https://doi.org/10.5194/egusphere-2023-1224
Preprint. Discussion started: 9 June 2023

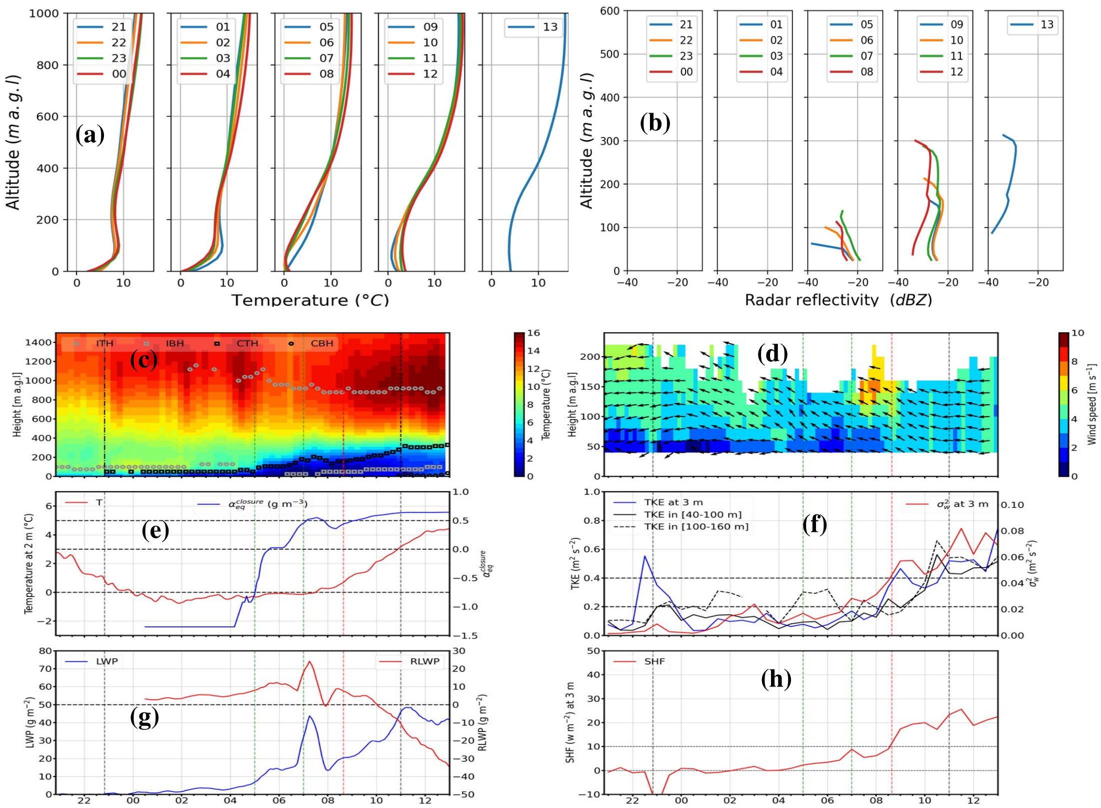

Figure 4: Evolution of fog macrophysical characteristics observed on the 28-29 December 2019 (case study 1, IOP 5) at Charbonnière. In (a-b) vertical profiles of air temperature from the Hatpro microwave radiometer (MWR) and radar reflectivity from Basta radar, respectively. In (c) time-height cross-section of air temperature from the MWR (shaded), time evolution of inversion top height (ITH) (open gray squares), inversion base height (IBH) (open gray squares), cloud top height (CTH) from the cloud radar (open black squares), and the cloud base height (CBH) from the Celiometer (open black circles). In (d) wind speed (shaded) and direction (arrows) from the WindCube. Arrows in (d) indicate only the direction of the horizontal flow. Time evolution of (e) air temperature at 3 m a.g.l from the meteorological station (red line) and equivalent adiabaticity of closure from the fog conceptual model (blue line), (f) the mean of the turbulent kinetic energy (TKE) in the layer 40 – 220 m for the WindCube (black line) and the TKE (blue line) and vertical velocity variance (red line) at 3 m a.g.l from the flux station at Charbonnière, (g) the LWP estimate from the MWR (blue line), the RLWP from the fog conceptual model (red line), and (h) sensible heat fluxes (SHF) (red and blue lines, respectively) from the flux station. Vertical black dashed lines indicate fog formation and dissipation times. Green dashed lines indicate the transition period (fog mature phase) from stable to adiabatic fog. The red dashed line indicates sunrise.

https://doi.org/10.5194/egusphere-2023-1224
Preprint. Discussion started: 9 June 2023

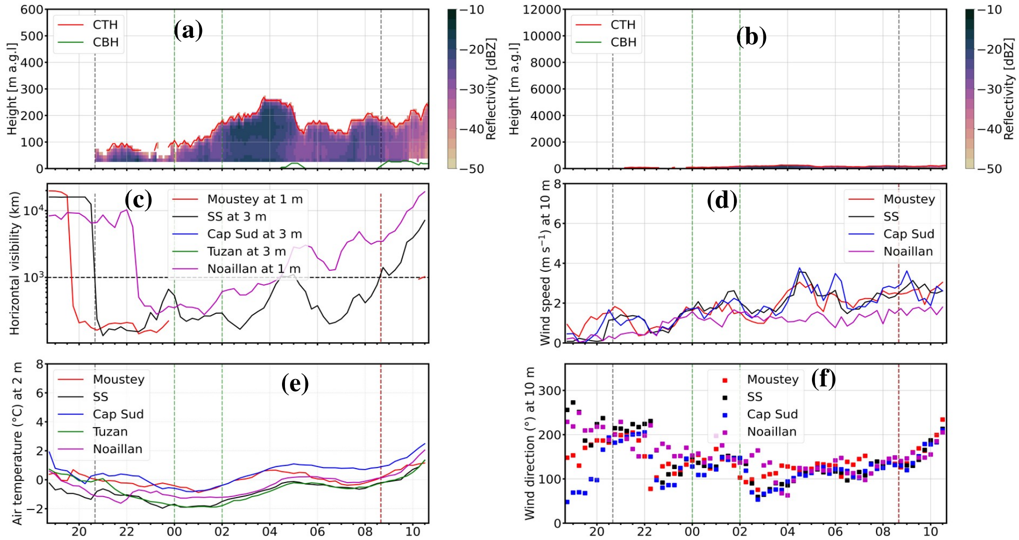

1035 **Figure 5:** As in Figure 3 but for the 5-6 January 2020 (case study 2, IOP 6). In (c), only
1036 Charbonnière and Noaillan have valid data. In (c), the visibility measured at Moustey, Tuzan and
1037 Cape Sud were interrupted by technical issues.

https://doi.org/10.5194/egusphere-2023-1224
Preprint. Discussion started: 9 June 2023

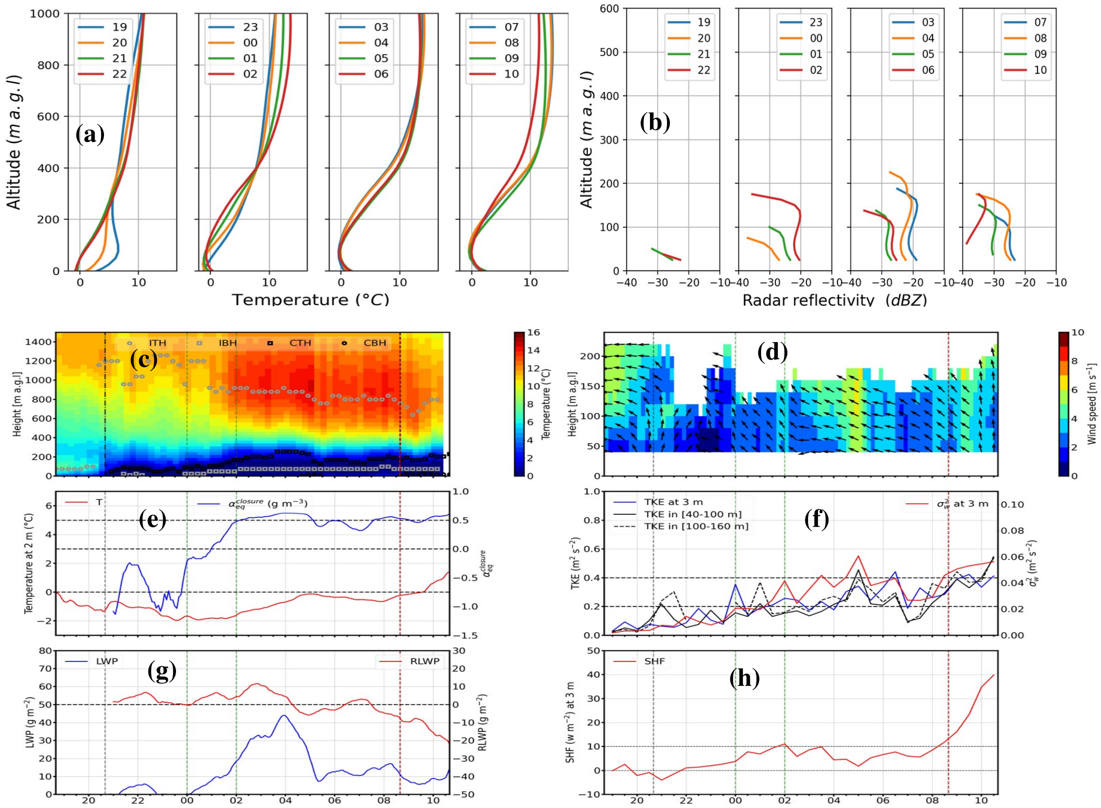

1038 **Figure 6:** As in Figure 4 but for the 5-6 January 2020 (case study 2, IOP6). The red vertical dashed
1039 line indicates the sunrise.

https://doi.org/10.5194/egusphere-2023-1224
Preprint. Discussion started: 9 June 2023

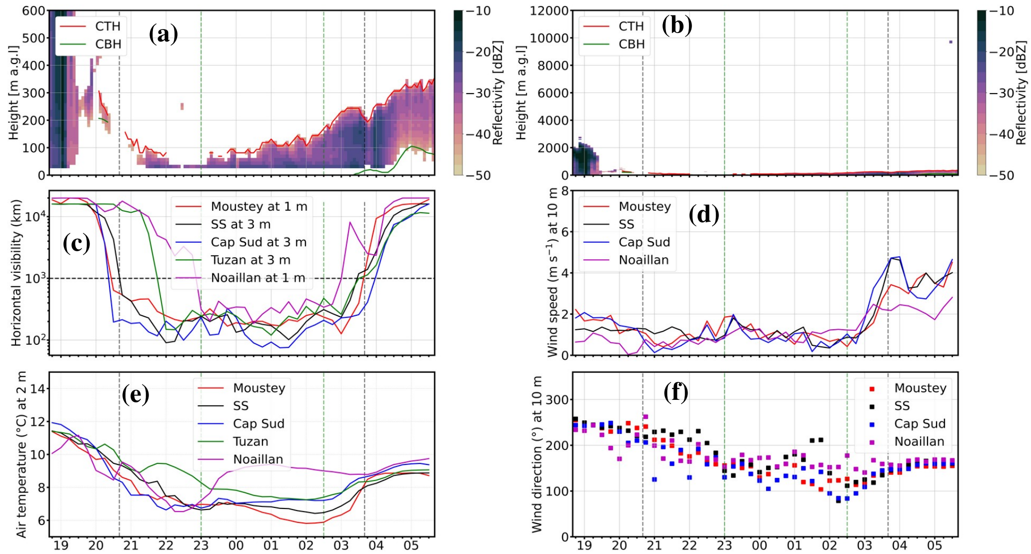

Figure 7 : As in Figure 3 but for the 8-9 February 2020 (case study 3, IOP 11)

https://doi.org/10.5194/egusphere-2023-1224
Preprint. Discussion started: 9 June 2023

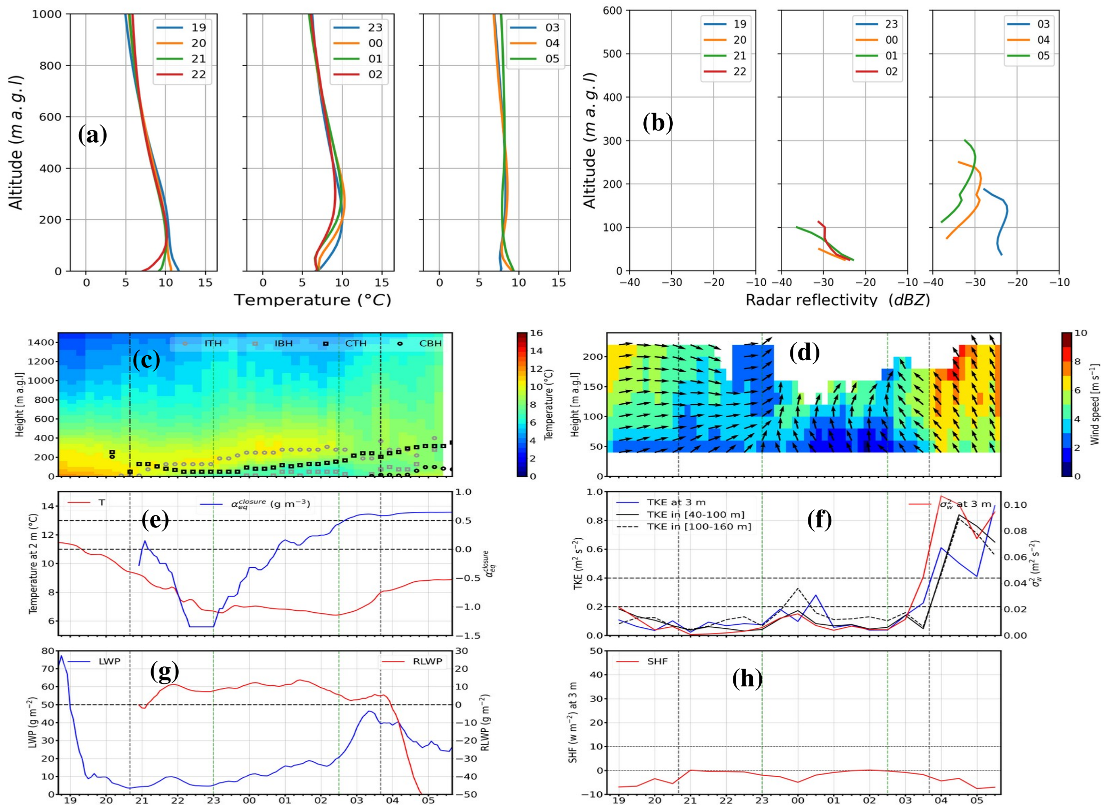

1041 **Figure 8:** As in Figure 4 but for the 8-9 February 2020 (case study 3, IOP 11).

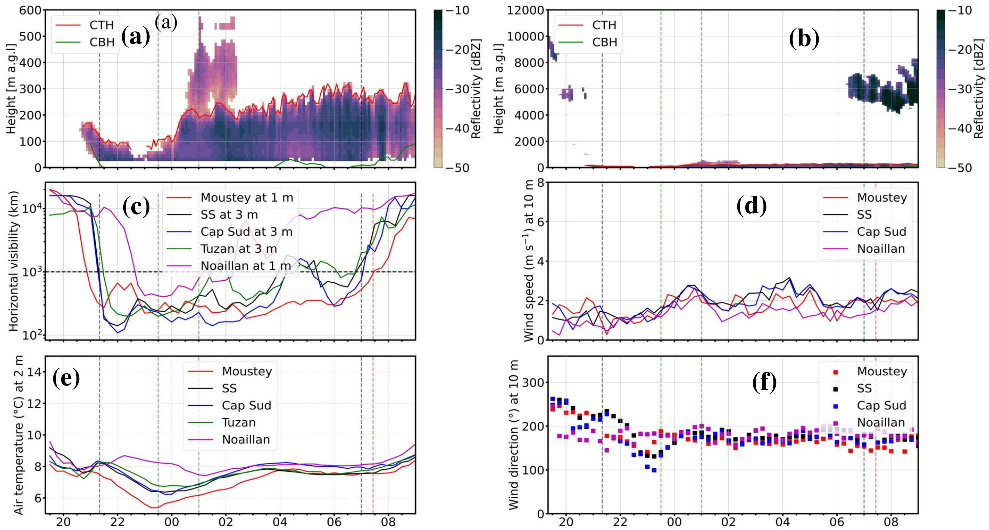

1042 **Figure 9 :** As in Figure 3 but for the 7-8 March 2020 (case study 4, IOP 14).

https://doi.org/10.5194/egusphere-2023-1224
Preprint. Discussion started: 9 June 2023

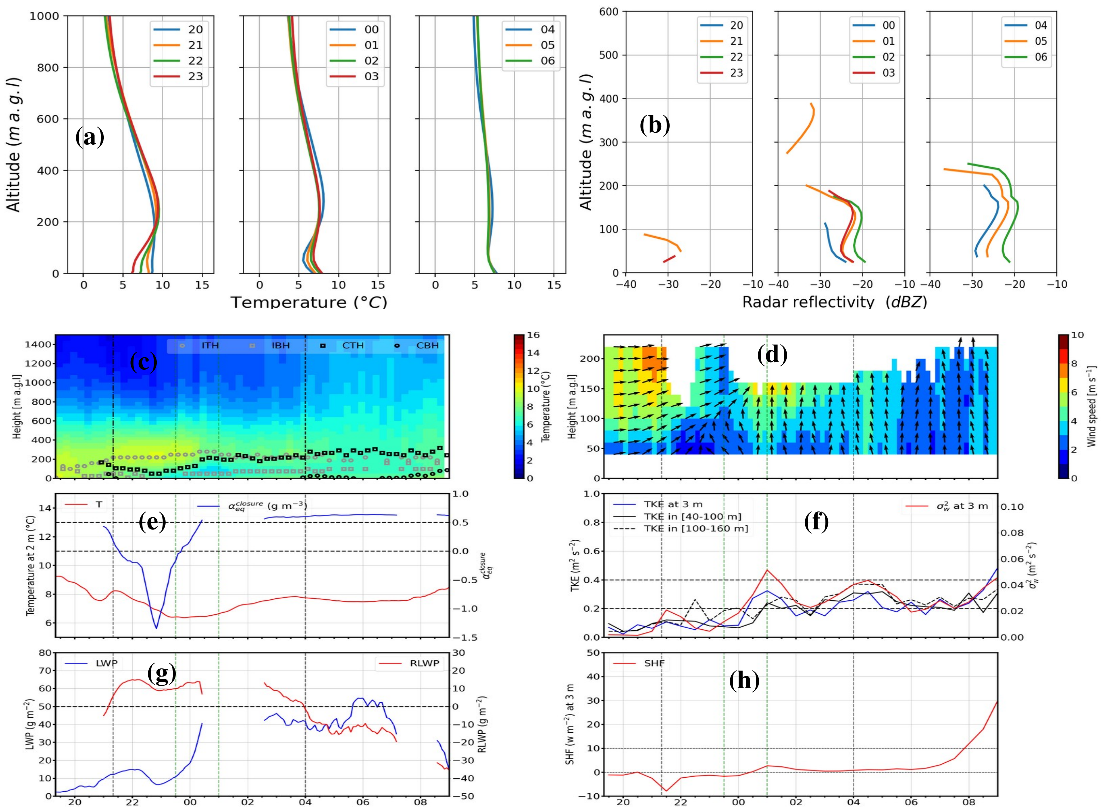

1043 **Figure 10 :** As in Figure 4 but for the 7-8 March 2020 (case study 4, IOP 14). The LWP, RLWP,
1044 and $\alpha_{eq}^{closure}$ are disrupted between 00:30 and 02:30 UTC because the LWP estimated by the MWR
1045 take into account the liquid water in the advected stratus.

https://doi.org/10.5194/egusphere-2023-1224
Preprint. Discussion started: 9 June 2023

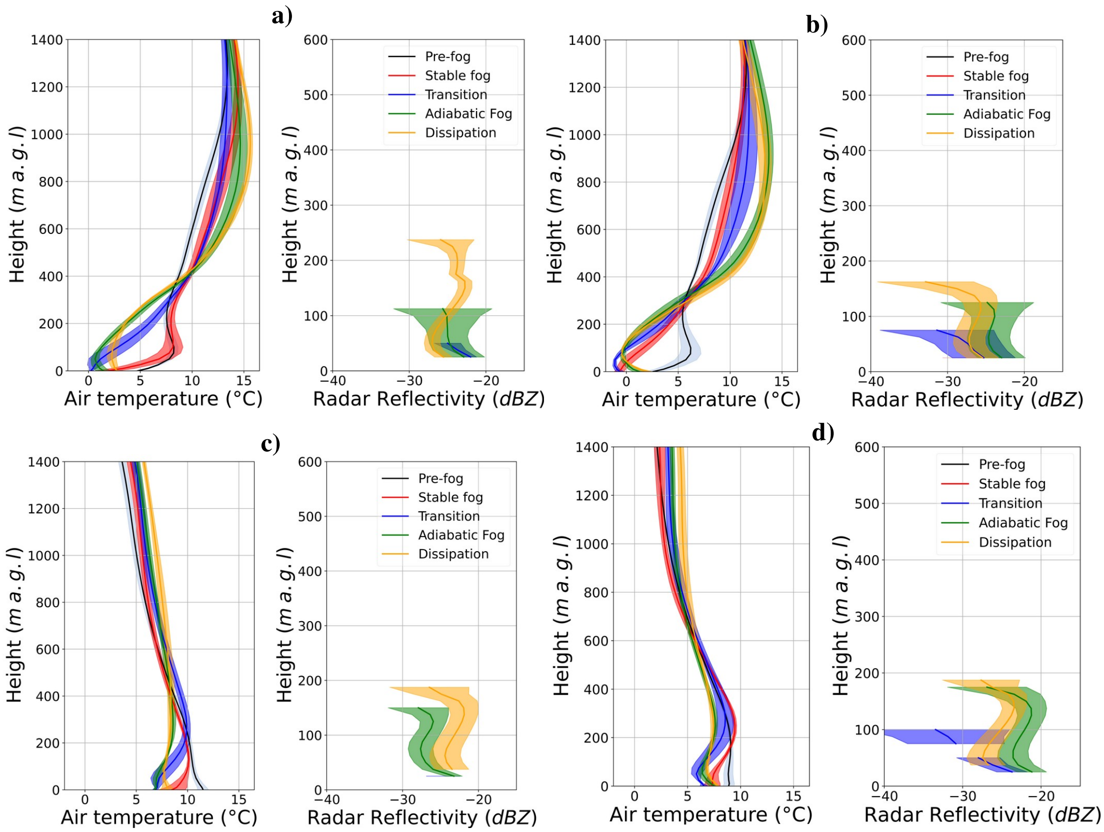

1046 **Figure 11:** Vertical profiles of air temperature and radar reflectivity put together for each fog case study (a) for case 1,
1047 (b) case 2, (c) case 3 and (d) case 4. Line and shaded area indicate the mean and standard deviation of air temperature
1048 and radar reflectivity during each fog phase.